Title
More Realistic Intermediate Depth Dry Firn Densification in the Energy Exascale Earth System Model (E3SM)

Journal
Journal of Advances in Modeling Earth Systems, 14(3)

ISSN
1942-2466

Authors
Schneider, Adam M
Zender, Charles S
Price, Stephen F

Publication Date
2022-03-01

DOI
10.1029/2021ms002542

More Realistic Intermediate Depth Dry Firn Densification in the Energy Exascale Earth System Model (E3SM)

Adam M. Schneider[1], Charles S. Zender[1], and Stephen F. Price[2]

[1]University of California, Irvine, Department of Earth System Science, Croul Hall, Irvine, CA 92697-3100
[2]Fluid Dynamics and Solid Mechanics Group, Los Alamos National Laboratory, Los Alamos, NM 87545

Key Points:

- We intercompare three snow density parameterizations and their effects on firn simulated in E3SM's land model (ELM).
- Incorporating a two-stage firn densification model into ELM improves densities at depths of 20 to 60 m.
- Applied to Greenland and Antarctica, improving 20 to 60 m depth dry firn density decreases firn air content by more than 20%.

Corresponding author: Adam Schneider, amschnei@uci.edu

Abstract

Earth system models account for seasonal snow cover, but many do not accommodate the deeper snowpack on ice sheets (aka firn) that slowly transforms to ice under accumulating snowfall. To accommodate and resolve firn depths of up to 60 m in the Energy Exascale Earth System Model's land surface model (ELM), we add 11 layers to its snowpack and evaluate three dry snow compaction equations in multi-century simulations. After comparing results from ELM simulations (forced with atmospheric reanalysis) with empirical data, we find that implementing into ELM a two-stage firn densification model produces more accurate dry firn densities at intermediate depths of 20 to 60 m. Compared to modeling firn using the equations in the (12 layer) Community Land Model (version 5), switching to the two-stage firn densification model (with 16 layers) significantly decreases root-mean-square errors in upper 60 m dry firn densities by an average of 41 kg m^{-3} (31%). Simulations with three different firn density parameterizations show that the two-stage firn densification model should be used for applications that prioritize accurate upper 60 m firn air content (FAC) in regions where the mean annual surface temperature is greater than roughly -31°C. Because snow metamorphism, firn density, and FAC are major components in modeling ice sheet surface albedo, melt water retention, and climatic mass balance, these developments advance broader efforts to simulate the response of land ice to atmospheric forcing in Earth system models.

Plain Language Summary

Massive ice sheets cover Earth's largest island (Greenland) and the Antarctic continent. A large fraction of their surfaces consists of multi-year snow, known as firn, which goes through the process of densification after falling from the atmosphere. Until now this fundamental process in glaciology has yet to be accounted for in the U.S. Department of Energy's Earth System Model (E3SM). Here we enhance E3SM's snowpack model to accommodate greater firn depths on ice sheets. Our results demonstrate a new capability in an Earth system model, i.e., calculating firn density as deep as 60 m below the surface. Our developments in E3SM combine both seasonal snow and firn processes to advance broader efforts towards simulating ice sheet evolution and sea level rise in Earth system models.

1 Introduction

Since the end of the twentieth century, global mean sea level continues to rise at an accelerating rate due to, in part, mass loss from the surface of the Greenland Ice Sheet (GrIS) (WCRP Global Sea Level Budget Group, 2018; M. R. van den Broeke et al., 2016). As the GrIS surface warms, regional climate models are being employed to study processes involved in its climatic mass balance, essentially the difference between mass accumulation (primarily from snowfall) and mass loss (primarily from melt and runoff) near the surface (Noël et al., 2018; Fettweis et al., 2017; van Angelen et al., 2014). Because of their superior horizontal resolution, regional climate models can resolve topographic features that determine the prevailing specific (local) surface mass balance processes. However, predicting future GrIS surface mass loss and its contribution to global mean sea level rise relies on Earth system models coupled to dynamic ice sheet components (Lenaerts et al., 2019; Muntjewerf et al., 2020). Because of the subgrid-scale topographic features and complex interactions between the atmosphere and ice sheet surface, ice sheet climatic mass balance is challenging to represent in Earth system models and depends on complex snowpack modules that include surface melt, water percolation, refreezing, and other densification mechanisms (Fyke et al., 2018; Vizcaino, 2014).

Although there are highly complex snowpack models capable of simulating alpine (and seasonal) snow conditions (Tuzet et al., 2017; Krinner et al., 2018), they generally do not include realistic metamorphism for the entire range of multi-year snow (aka *firn*) densities ($\sim$ 200 to 830 kg m^{-3}) or are not computationally affordable in an Earth system model (e.g., Hagenmuller et al., 2015). In a recent development, Stevens et al. (2020) apply their Community Firn Model to test 13 firn densification models, which produce plausible density-versus-depth relationships for the regions where they were calibrated. Even with consistent surface boundary conditions, the models produce a wide range of firn air content (FAC), which is mostly attributed incomplete representations of microphysical processes (Lundin et al., 2017). Despite their inconsistencies, incorporating a firn densification model into an Earth system model adds a new capability for climatic mass balance studies, which require the capacity to accommodate a realistic FAC. Recent advances in the Community Earth System Model version 2 (CESM2) lead the effort to study climatic mass balance processes in Earth system models (van Kampenhout et al., 2020; Sellevold & Vizcaíno, 2020; Lenaerts et al., 2020). While these advances represent a new frontier in Earth system modeling, the study by Stevens et al. (2020) implies that the CESM2 firn density parameterization, which uses the mountain snowpack compaction model of Vionnet et al. (2012), results in a total FAC that is too high.

If there exists a total FAC bias in CESM2, then it poses the problem of how to develop the firn in an Earth system model without the potential to misdiagnose melt percolation, refreezing and runoff, which depend on pore space in firn. Addressing this problem is vital to accurately calculate future GrIS climatic mass balance, where rapid climate change will continue expanding melt extent into formerly dry snow areas. Moreover, because no particular firn densification model has been validated for global applications, the principal question of which compaction equation to incorporate into an Earth system model remains difficult to address. Here we adapt the land snow metamorphism routine in the Energy Exascale Earth System Model (E3SM) (Golaz et al., 2019) to accommodate more realistic intermediate-depth (10 to 60 m) dry firn densities.

Our overarching objective is to expand and assess in E3SM's Land Model (ELM) the FAC in dry-snow zones, where the complex effects of liquid water in firn (Steger et al., 2017) can be neglected. In section 2, we summarize two approaches commonly used to model snow metamorphism and firn densification, which are similar processes but have different vertical scales ($\sim$1 m versus $\sim$100 m, respectively) of application. In section 3, we describe how aspects of the modeling approaches discussed in section 2 are combined in ELM and introduce a new, expanded layering scheme. In section 4, we compare dry firn densities in three ELM experiments to results from the established empirical model of Herron and Langway (1980) (henceforth HL80) and evaluate root mean square errors (RMSE) with respect to measurements from the Surface Mass Balance and Snow on Sea Ice Working Group (SUMup) dataset (Montgomery et al., 2018). In section 5, we discuss the extent to which using 16 layers and incorporating a two-stage firn densification model into the snow metamorphism routine in ELM improves 20 to 60 m dry firn densities and FAC. After concluding in section 6, we provide an appendix showing how to re-calibrate the snow metamorphism and firn densification expressions that will be used for fine-tuning density profiles in future, experimental versions of ELM and E3SM.

2 Background

The interior surface of a continental-scale ice sheet (i.e., Greenland or Antarctica) consists of large regions where intermediately dense layers of dry snow are progressively buried by new snowfall. This dry, porous part of an ice sheet, with older snow that is more commonly known as firn, compacts under its overburden pressure during a slow metamorphic process that eventually forms new glacial ice. The duration of this entire transformation, from new snow to bubbly ice, ranges from fewer than 200 to more than 2,000 years depending on environmental factors (e.g., initial snow density) and local climate conditions (e.g., temperature and new snow accumulation rate) (Herron & Langway, 1980; Cuffey & Paterson, 2010).

Depending on their applications, numerical models that include metamorphic processes relevant to the transformation of snow to ice can be divided into two general categories. These categories include seasonal snowpack models, which calculate compaction rates using the finite-element method (Podolskiy et al., 2013), and explicit firn densification models, which provide either an empirical density versus depth relationship or a dynamic formulation for densification rates given as a function of overburden pressure, local temperature, and density. Global snowpack models are more commonly used in Earth system models to simulate seasonal snow cover, which often do not include the essential processes governing densification rates for higher densities that typify firn.

2.1 Seasonal Snowpack in Earth System Models

Snow compaction in Earth system and land surface models is routinely represented by one-dimensional parameterizations of the general form

$$\dot{\epsilon} \equiv \frac{1}{\Delta z}\frac{\partial \Delta z}{\partial t} = -\frac{P}{\eta}, \tag{1}$$

which relates the vertical strain rate $\dot{\epsilon}$ [s^{-1}] (equivalent to the compaction rate of a layer with thickness Δz at time t) to the overburden (load) pressure P [Pa] via a dynamic viscosity function η [Pa s]. The load pressure function $P(z)$, calculated for each layer at a depth z with mass density ρ, is equal to the product of the acceleration due to gravity g (9.80665 m s^{-2}) and the depth-integrated (from the snow surface to z) areal (column) density $\sigma(z) = \int_0^z \rho(z)\,dz$ [kg m^{-2}].

As in the land component CLM4 of CESM (version 1) (Lawrence et al., 2011), the unmodified ELM (version 1) further represents snow strain rates as the sum of three terms representing: overburden pressure, as in eq. (1); *destructive metamorphism* (denoted by the subscript "dm"); and melt (Anderson, 1976). For each vertical layer, deformation due to overburden pressure is calculated by substituting into eq. (1) the dynamic viscosity equation

$$\eta = \eta_0 \exp\left[c_1(T_f - T) + c_2\rho\right], \tag{2}$$

with mass density ρ [kg m^{-3}], temperature T [K], and constants $T_f = 273.15$ K, $c_1 = 0.08$ K^{-1}, $c_2 = 0.023$ m^{3}kg^{-1}, and $\eta_0 = 8.8 \times 10^6$ kg m^{-1} s^{-1} [Pa s]. Snow layer temperatures $T(z)$ are calculated using an energy balance scheme in conjunction with an implicit finite difference (Crank-Nicolson) method (Jordan, 1991), and the radiative transfer of energy is simulated using the Snow, Ice, and Aerosol Radiative (SNICAR) model that also includes the evolution of the snow effective grain size r_e (Flanner & Zender, 2006; Flanner et al., 2007). Densification due to destructive metamorphism, which includes the settling and accretion of snow grains as they age, is calculated for each vertical layer as a temperature (T) dependent, piecewise-defined function of density (ρ), expressed as an additive engineering strain (strain rate) equivalent

$$\dot{\epsilon}_{\mathrm{dm}} = \begin{cases} -c_3 \exp[c_4(T - T_f)], & \text{if } \rho < \rho_{\mathrm{dm}} \\ -c_3 \exp[c_4(T - T_f) - c_5(\rho - \rho_{\mathrm{dm}})], & \text{if } \rho \geq \rho_{\mathrm{dm}} \end{cases}, \tag{3}$$

with constants $c_3 = 2.78 \times 10^{-6}$ s^{-1}, $c_4 = 0.04$ K^{-1}, $c_5 = 46 \times 10^{-3}$ m^{3}kg^{-1}, and a density threshold ρ_{dm} (100 kg m^{-3}) above which the strain rate tapers off.

In CLM5, the dynamic viscosity equation η was updated according to Vionnet et al. (2012), which is expressed as

$$\eta = f_1 f_2 \eta_0 \frac{\rho}{c_\eta} \exp\left[a_\eta(T_f - T) + b_\eta\rho\right], \tag{4}$$

with constants $a_\eta = 0.1$ K^{-1}, $b_\eta = 0.023$ m^{3}kg^{-1}, and $\eta_0 = 7.47499 \times 10^7$ kg m^{-1} s^{-1} [Pa s]. We note here that there exists a discrepancy in the literature regarding the units of η_0, resulting in the above value given as $\eta_0 = g\eta_0^*$, where $\eta_0^* = 7.62237 \times 10^6$ kg s m^{-2}.

This updated viscosity equation in CLM5 contains the adjustable coefficient $(f_1 f_2)/c_\eta$, with $c_\eta = 450$ kg m^{-3}, $f_2 = 4.0$, and a function f_1 that depends on (and is equal to unity in the absence of) liquid water content, whereas Vionnet et al. (2012) include a grain size dependence in the formulation of f_2. The destructive metamorphism expression in CLM5, eq. (3) but with an increased density threshold tapering parameter ρ_{dm} (from 100 to 175 kg m^{-3}), is added to eq. (1) with the updated dynamic viscosity from eq. (4). In the study by van Kampenhout et al. (2017), a wind speed dependence is introduced into the initial snow density function in CLM4, which improves snow densities at the surface of ice sheets. To further improve ice sheet surface (and near-surface) densities, van Kampenhout et al. (2017) also add a new densification term to the compaction model that incorporates compaction due to drifting snow. Their results also eliminate a -7.6 m bias (too shallow) in the depth where the bulk density reaches 550 kg m^{-3}. This "characteristic depth ," defined as the depth at which density is equal to 550 kg m^{-3}, represents the transition from the first to the second stage of firn densification (Herron & Langway, 1980). Despite their advances, however, van Kampenhout et al. (2017) also demonstrate that upper 1 m ice sheet densities and characteristic firn depths simulated with CLM5 are only weakly spatially correlated ($R^2 = 0.15$) with observations. Furthermore, this particular CLM5 firn density paramterization possibly results in an erroneous stagnation of the intermediate-stage firn densification, marked (crudely) by densities in the range of 550 to 830 kg m^{-3} (Stevens et al., 2020). While plausible physical explanations supporting this concept of distinct stages of densification exist, the delineation of stages is applied in firn densification models to better accommodate transitions that are apparent at approximate critical densities.

2.2 Firn Densification Models

Empirical firn densification models have historically employed analytic functions that assume a steady-state density profile. They commonly define a critical density (usually 550 kg m^{-3}) that separates two stages of densification. Herron and Langway (1980), for example, demonstrate how their model (HL80) can predict observed density-depth relationships for these first two stages given the mean annual temperature, annual accumulation rate, and surface density.

When the climate is stationary, mean annual temperatures and accumulation rates are stable, eventually leading to firn well-approximated by the steady-state condition. Assuming a steady-state, consider a small parcel of firn with a vertical velocity w [m s^{-1}] relative to the surface, such that

$$w(z) \approx \frac{A}{\rho(z)} \tag{5}$$

where A is the mean accumulation rate [kg m^{-2} s^{-1}] (equivalent to mm SWE s^{-1}) and $\rho(z)$ is the bulk density [kg m^{-3}] of firn at a given depth z [m] (Bader, 1954). Neglecting wind shear, the one-dimensional (kinematic) densification rate can be expressed by the material derivative

$$\frac{D}{Dt}\rho(z,t) = \frac{\partial \rho}{\partial z} w(z,t) + \frac{\partial \rho}{\partial t}, \tag{6}$$

with $\partial\rho/\partial t \approx 0$ in a steady-state. Substituting the right hand side of eq. (5) for $w(z,t)$ in eq. (6) gives an estimate of the advective densification rate, which is closely related to the volumetric strain rate $\dot{\epsilon}$ via

$$-\frac{1}{\rho}\frac{D}{Dt}\rho(z) \approx -\frac{A}{\rho(z)^2}\frac{d\rho}{dz} \approx \frac{dw}{dz} \equiv \dot{\epsilon}. \tag{7}$$

This steady-state approach is useful for deriving realistic density profiles and vertical strain rates in dry snow zones, but does not provide a dynamic representation of physical processes simulated in modern Earth system models.

A dynamic, numerical densification model integrates compaction rates for each snow element on a multi-layer, vertical grid. For example, Arthern et al. (2010) and Ligtenberg et al. (2011) developed and tuned (respectively) a semi-empirical two-stage model based on measured firn thinning rates that can be coupled to the heat equation to calculate time dependent densification rates. Accordingly, the densification rate $\partial\rho/\partial t$ can be expressed in terms of temperature T, bulk density ρ, overburden pressure P, and an effective snow grain radius r_e, such that

$$\frac{1}{\rho}\frac{\partial\rho}{\partial t} = \frac{k_c \exp\left(\frac{-E_c}{RT}\right)\left[\frac{\rho_i}{\rho} - 1\right] P}{r_e^2}, \tag{8}$$

with activation energy E_c (60 kJ mol^{-1}), universal gas constant R (8.31 J K^{-1} mol^{-1}), ice density ρ_i (917 kg m^{-3}), and $k_c = 9.2\times10^{-9}$ kg^{-1}m^{3}s for $\rho \leq 550$ kg m^{-3} or $k_c = 3.7\times10^{-9}$ kg^{-1}m^{3}s for $\rho > 550$ kg m^{-3}. Adjustment of the rate coefficient k_c for $\rho \leq 550$ kg m^{-3} is necessary to capture greater densification rates during the first stage of densification possibly explained by grain-boundary sliding (Alley, R. B., 1987). Because the model is calibrated to measurements confined to sites on or near the relatively warm Antarctic Peninsula, however, it should not be applied in Earth system models to represent the cold interior regions of Greenland and Antarctica without further evaluation. Such an evaluation is performed in this study.

3 Data and Methods

3.1 Snowpack Model Development and Experimental Densification Parameterizations

To test how well snow metamorphism implementations in Earth system models can accommodate realistic firn densities, two necessary changes were first applied in ELM(v1). Necessary changes include the increase in maximum allotted SWE (capped at 1 m in the standard ELM) and the increase in the maximum number of snow layers (originally 5), which were implemented into development versions of the code along with succeeding modifications as described below. The following sections delineate three experimental firn densification configurations ("vK17", "A10", and "vK17+") with both the necessary changes and unique corresponding modifications fully implemented into ELM.

3.1.1 vK17: Updates to ELM from CLM5

Our modifications in E3SM began with the snow model in ELM(v1), which was inherited from the CLM(v4.5) used in CESM(v1). Guided by firn model improvements in CLM(v5) and used in CESM(v2) (van Kampenhout et al., 2017; Lawrence et al., 2019), we increased the maximum number of snow layers from 5 to 12. For the purpose of comparing new experimental results from ELM to those from the CLM5 firn density parameterization, we adopted the same 12 layer grid from van Kampenhout et al. (2017) and implemented into ELM the overburden compaction model from Vionnet et al. (2012), using eq. (1) with the dynamic viscosity function from eq. (4). We also set the destructive metamorphism (dm) density threshold $\rho_{\mathrm{dm}} = 175$ kg m^{-3} in eq. (3). Equipped with this 12 layer vertical snowpack grid, the simulation of firn densification is accommodated in ELM by increasing the maximum allotted SWE from 1 m to an arbitrarily large value (10,000 m).

In ELM(v1), initial (i.e., fresh) snow density is solely a function of the surface temperature and is independent of the wind speed. This temperature-only dependence is a model deficiency that contributes to ice sheet surface densities that are too low. To improve ice sheet surface densities, two updates from CLM5 were implemented into ELM. These include a wind speed dependence in the fresh snow density parameterization and the addition of a densification term that incorporates compaction (up to 350 kg m^{-3}) due to drifting snow (as in eqs. 2–4 and 9–13, respectively, from van Kampenhout et al. (2017)). This configuration is consistent with and fully described by van Kampenhout

Table 1. Minimum and maximum layer thicknesses (meters) used in the vK17, A10, and vK17+ firn densification experiments. The dynamic grid can, based on the total snowpack thickness, adjust every time-step the total number of layers N (maximum of 12 or 16) and the bottom two layers' thicknesses. Maximum layer thicknesses depend on if the particular layer is, at a given time-step, the bottom layer (i.e., if $N = k$).

	vK17[a]			A10 (and vK17+)		
Layer (k)	$\Delta z_{\min}$	$\Delta z_{\max}^{N=k}$	$\Delta z_{\max}^{N>k}$	$\Delta z_{\min}$	$\Delta z_{\max}^{N=k}$	$\Delta z_{\max}^{N>k}$
1 (top)	0.010	0.03	0.02	0.010	0.03	0.02
2	0.015	0.07	0.05	0.015	0.07	0.05
3	0.025	0.18	0.11	0.025	0.18	0.11
4	0.055	0.41	0.23	0.055	0.41	0.23
5	0.115	0.88	0.47	0.115	0.88	0.47
6	0.235	1.83	0.95	0.235	1.83	0.95
7	0.475	3.74	1.91	0.475	3.74	1.91
8	0.955	7.57	3.83	0.955	7.57	3.83
9	1.915	15.24	7.67	1.915	15.24	7.67
10	3.835	30.59	15.35	1.915	15.24	7.67
11	7.675	61.30	30.71	1.915	15.24	7.67
12	15.355	∞	n/a	1.915	15.24	7.67
13	n/a	n/a	n/a	1.915	15.24	7.67
14	n/a	n/a	n/a	1.915	15.24	7.67
15	n/a	n/a	n/a	1.915	15.24	7.67
16 (bottom)	n/a	n/a	n/a	1.915	∞	n/a

[a]From van Kampenhout et al. (2017).

et al. (2017), which we refer to here as "vK17." Results from this experiment show how the CLM5 firn model performs in ELM(v1).

3.1.2 A10: Enhanced Layering Scheme with a Two-Stage Firn Densification Model

After adopting the changes introduced into CLM5 by van Kampenhout et al. (2017), we expanded and modified their 12 layer snowpack scheme to further improve the vertical resolution at firn depths of 10 to 60 m. Expanding to 16 layers, minimum and maximum layer thicknesses were modified to resolve firn densities at a vertical resolution of 7.67 m (Table 1). The upper-most nine layers vary in their minimum and maximum allotted thicknesses and conform to the upper nine layers used in the 12 layer grid described by van Kampenhout et al. (2017). If the snowpack becomes deep enough to fill the upper 15 layers, a semi-infinite 16th (bottom-most) layer is created. This improved spatial resolution is necessary to better simulate relevant processes at intermediate depths and overburden pressures more typical of firn. It also maintains the variable spacing near the snowpack surface that is needed to resolve high temperature gradients and to accurately model solar radiative transfer.

Next, compaction due to the overburden pressure from snow loading was changed according to Arthern et al. (2010) by replacing eq. (1) with eq. (8). In this experiment ("A10"), the overburden pressure (or load) is represented by the *grain-load stress*, which is given by

$$P = g\left(\frac{\rho_i}{\rho}\right)\sigma, \tag{9}$$

Table 2. ELM dry firn densification parameterization. The A10, vK17, and vK17+ experiments use a maximum of 12 or 16 snow layers (N) and include compaction due to destructive metamorphism, calculated from eq. (3) with various coefficients (c_3) and density thresholds (ρ_{dm}), plus overburden pressure compaction, calculated with either eq. (1) or eq. (8) as a function of layer temperature (T), density (ρ), and columnar mass density (σ) as shown. In vK17+, an additional term not shown in the table, from eq. (10), is included (for $r_e < 0.08$ mm) representing compaction (and gravitational settling) of dendritic snow. Numerical values of the constants provided (and their units) are provided in Section 2 or are noted below.

Label	N	c_3 (s^{-1})	ρ_{dm} (kg m^{-3})	Overburden compaction^a (s^{-1})
A10^b	16	2.78×10^{-6}	175	$(-k_c/r_e^2)\exp\left(\frac{-E_c}{RT}\right)\left[\frac{\rho_i}{\rho}-1\right] g \left(\frac{\rho_i}{\rho}\right)\sigma$
vK17^c	12	2.78×10^{-6}	175	$(-4\eta_0^*)^{-1}\exp\left[a_\eta(T-T_f)-b_\eta\rho\right]\left(\frac{c_\eta}{\rho}\right)\sigma$
vK17+^{cd}	16	0.83×10^{-6}	150	$(-4.9\eta_0^*)^{-1}\exp\left[a_\eta(T-T_f)-b_\eta\rho\right]\left(\frac{c_\eta}{\rho}\right)\sigma + c_6$

^{a} With $\sigma(z) = \int_0^z \rho(z)\,dz$ (kg m^{-2}).
^{b} See text following eq. (8) for numerical constants.
^{c} See text following eq. (4) for numerical constants (T_f = 273.15 K).
^{d} With c_6 = -1.18 × 10^{-10} s^{-1}.

where σ [kg m^{-2}] is the vertically integrated column density and g [m s^{-2}] is the acceleration due to gravity. The factor ρ_i/ρ (pure ice density ρ_i divided by snow bulk density ρ) is included because only the grains, not the pore space, support the load (Cuffey & Paterson, 2010). This experiment uses our new 16 layer grid and also includes the changes discussed in vK17 that result in improvements to ice sheet surface densities (fresh snow density and wind drift compaction improvements) and the density threshold ρ_{dm} set equal to 175 kg m^{-3}, as in vK17. The fundamental distinctions between the vK17 and A10, plus a similar follow-on configuration (vK17+) are summarized in Table 2.

3.1.3 vK17+: Follow-on experiment

Following the vK17 and A10 experiments, an additional firn density parameterization, "vK17+," was tested in ELM to reduce biases found in vK17 (as shown below in Section 4). For this purpose, statistical modeling was used to estimate empirical compaction rates from HL80, which were then used to calibrate the vK17+ densification parameters c_3, from eq. (3), and f_2, from eq. (4) (see Appendix for more details). The resulting vK17+ configuration is similar to vK17 with five subtle but important distinctions (Table 2). These distinctions are: the number of layers, i.e., 12 in vK17 versus 16 in vK17+; the value of the destructive metamorphism coefficient c_3, from eq. (3), modified from 2.777 × 10^{-6} s^{-1} in vK17 to 0.83 × 10^{-6} s^{-1} in vK17; the value of the destructive metamorphism density threshold parameter ρ_{dm}, modified from 175 kg m^{-3} in vK17 to 150 kg m^{-3} in vK17+ (adhering to Anderson, 1976); the value of the overburden pressure compaction correction factor f_2, modified from 4.0 in vK17 to 4.9 in vK17+; and an additional constant compaction term (c_6 = -1.18 × 10^{-10} s^{-1}) added to eq. (1) for vK17+. The vK17+ configuration also includes an additional fresh snow compaction term calibrated specifically for dendritic snow (Lehning et al., 2002), expressed as

$$\dot{\epsilon}_{\mathrm{dendritic}} = \frac{-g\sigma}{0.007\rho^{4.75-T_c/40}} \tag{10}$$

as a function of vertically-integrated column density σ [kg m^{-2}], snow density ρ [kg m^{-3}], and snow temperature T_c in °C. Because ELM does not specify snow grain shape or type, we added this term only for snow having a low-enough snow grain size (i.e., where its layer-dependent optical sphere equivalent radius $r_e < 0.08$ mm) to be considered dendritic. This additional compaction term $\dot{\epsilon}_{\text{dendritic}}$ did not have a noticeable effect on the density profile deeper than 1 m.

3.2 ELM Simulations

To solve for firn densities representative of each experimental configuration, rather than an arbitrary initial condition, each experiment started with a lengthy (260 year) spin-up period that integrated compaction rates while accumulating snowfall into ELM's snowpack module. After implementing into ELM the three experimental firn density configurations (i.e., vK17, A10, and vK17+) described above, the Common Infrastructure for Modeling the Earth (CIME) was used to setup, build, and run each configuration as a stand-alone land model. In this ELM "stand-alone" mode, atmospheric re-analyses (0.5° resolution) provide the surface boundary conditions that include 6-hourly varying precipitation, solar radiation, temperature, and wind speed from the Climate Research Unit and the National Center for Environmental Prediction (CRUNCEP) (Viovy, 2018). Historical climate simulations were initialized in the following manner using a coarse horizontal-resolution (500 km) ELM grid ("I-compset" with "ne11" grid). Limited computational resources prevented us from conducting these multi-century integrations at higher resolutions. However, the coarse grid-scale adequately represents and preserves the important mean annual temperature and accumulation rate characteristics ($\bar{T} <$ -19° C; $A <$ 0.5 m SWE yr.$^{-1}$) for multiple interior grid-cells in the GrIS and AIS dry snow zones (Fig. 1). Beginning 1 January 1901, ELM's initial snowpack depth was set to 50 mm (SWE) over its pre-defined glaciated regions (which include most of Greenland and Antarctica) and everywhere north of 44° N to avoid absorbing excess radiation at the onset when there is typically snow cover. We then simulate 260 years with repeating (from 1901 to 1921), quasi-steady atmospheric conditions to integrate accumulating snow and simulate the process of firn densification. Overall, this initialization procedure (and "cold start" condition) removes any prior assumption about the natural firn density profiles and allows regions with at least 0.1 m SWE yr^{-1} of accumulation, after 260 years, to reach a total firn thickness of roughly 50 m.

Next, twentieth century simulations were initialized using conditions at the end of 260-year, repeating 1901–1921 climate simulations (i.e., as "restart runs") resulting in a near pre-industrial climate forcing (Fig. 1). One-hundred additional years of firn densification were simulated using the CRUNCEP atmospheric forcing dataset starting from 1901 and ending in 2001. In total, this combined procedure gives 360 years of snow accumulation and densification ending on 1 January 2001, with results differing only with respect to the specifics of the snowpack model used by ELM (as described in section 3.1). These simulations enable direct comparisons of results from vK17, A10, and vK17+ with recent firn density measurements provided in the SUMup dataset (Montgomery et al., 2018) and form the crux of our dry firn model validation.

3.3 Model Evaluation

3.3.1 HL80 versus ELM: Steady-State Density Profiles

To evaluate firn densities simulated in ELM, steady-state density profiles were calculated from the empirical model of HL80 and compared to results from the vK17, A10, and vK17+ experiments. Guided by the climate conditions applied at the Greenland and Antarctic ice sheets' surfaces (Fig. 1) and the studies of Fausto et al. (2018) and M. van den Broeke (2008), independent arrays of various mean annual temperatures (-34, -28, -22°C) , accumulation rates (0.1, 0.2, 0.3, 0.4, 0.5 m SWE yr^{-1}) and surface densities (270, 280, . . . , 360 kg m^{-3}), representative of ice sheets' relatively warm dry-snow zones (Vandecrux et al., 2019), were plugged into the analytic formulation of HL80. This method gives a range of steady-state density profiles representative of Greenlandareas with lower accu-

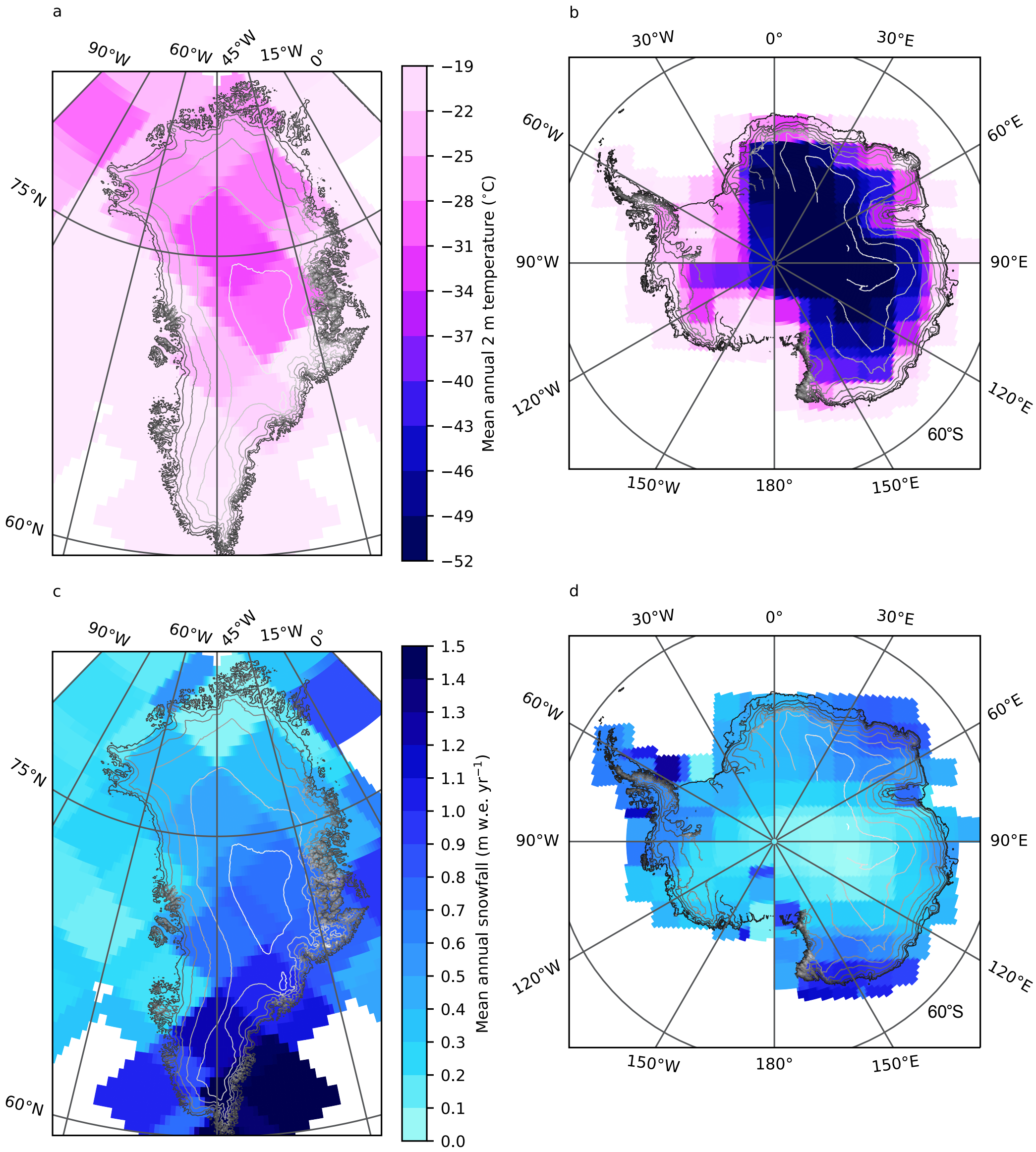

Figure 1. Greenland (a, c) and Antarctica (b, d) 1901–1921 climate forcing (from CRUNCEP) in ELM simulations. ELM nodes, centered within gridcells, are located at regular intervals of 500 km. Maps shown (at different scales) use the Lambert azimuthal equal-area projection. Elevation contours at 500 m intervals are generated using data from Howat et al. (2014) (for Greenland) and from Bamber et al. (2009) (for Antarctica).

mulation rates (northern regions) and Antarctica's warmer interior regions. Because of ELM's initial condition (50 mm SWE), which require simulations to build their own firn, density profiles in ELM are assumed quasi-steady (i.e., growing deeper but with otherwise small interannual variations) during the spin-up period while the climate forcing is repeatedly cycling over a 20-year (1901-1920) period. After 280 simulation years (each with 365 days), average ELM firn densities are calculated (from years 260–280) for dry snow only by first masking out all gridcells where maximum snowpack temperature (during the averaging period) exceeds 273.12 K. Data are then sorted by surface mean annual temperature, masked out where accumulation rates exceed 0.5 m SWE yr^{-1}, and finally compared with the range of empirical density profiles generated from HL80 for mean annual temperatures $\bar{T}$ = -34, -28, and -22°Cas described above. Sorting ELM data in this manner enables direct comparisons with HL80 model solutions in a common domain of temperature-accumulation rate sub-spaces independent of geographic location. This procedure is hence carried out to identify firn model biases that are independent from geographic errors in ELM induced by potentially inaccurate climate forcing data.

3.3.2 SUMup versus ELM: End of 20th Century Density Profiles

The Greenland and Antarctic ice sheet (AIS) dry snow zones were selected for our primary study domain because their vast horizontal length scales allow them to be more easily represented by low resolution (500 km) ELM simulations. A suitable time period for evaluation starts in 1980, marking the start of a 30 year period during which numerous firn density measurements included in the comprehensive SUMup dataset (Montgomery et al., 2018) were conducted on both ice sheets. Geographically, ELM grid-cells contain nodes that specify their latitude and longitude coordinates and contain time-varying bulk densities given for each snowpack layer. These time-varying simulated densities were evaluated by computing root-mean-square errors (RMSE) against density measurements from firn cores taken from 1980 to 2010 provided in the SUMup dataset. While there exist GrIS density measurements taken prior to 1980 and measurements from both ice sheets taken after 2010, we found that almost all measurements that extend at least 60 m in depth and are within ELM's dry snow boundaries fall between the years 1980 and 2010. Due to the warming climate during the 20th century (Fig. 2), our ELM simulations are left with only a couple of gridcells over Greenland that remain completely dry for all three experiments throughout 1980–2000. As a result, the evaluation of GrIS densities versus SUMup measurements includes a temporal mismatch that cuts off ELM results after 1970. This caveat, while possibly biasing the evaluation (ELM firn too early and / or too cold), benefits the analysis by including more of ELM's dry snow gridcells in the comparison, which, as before, are restricted to where maximum snowpack temperature (during the averaging period) does not exceed 273.12 K. Because the 20th century climate forcing over the AIS remains relatively constant (Fig. 2), however, this caveat does not apply to the evaluation of AIS densities versus SUMup measurements, which is temporally consistent. In total, eliminating ELM data where melt occurred leaves 5 ELM grid-cells from Greenland and 18 ELM grid-cells from Antarctica in the vK17 (7 and 25 ELM grid-cells, respectively, in A10, and 1 and 17 ELM grid-cells, respectively, in vK17+) experiment that contain locations of available SUMup measurements.

To evaluate RMSE, we applied a sorting algorithm that determines each SUMup density measurement's representative simulated value in ELM. First, measurements conducted across the GrIS and AIS are grouped according to their nearest ELM node by computing the relevant location similarity (distance) matrix. After finding a nearest ELM density profile (in time and space), the midpoint depth of each measurement determines the ELM snowpack layer nearest in depth space, which contains the relevant simulated density. In this comparison, ELM density profiles are interpreted as step functions, so RMSE are calculated for every available measurement with respect to the discrete values simulated using the vertical snowpack grid in ELM. With some measurements on the

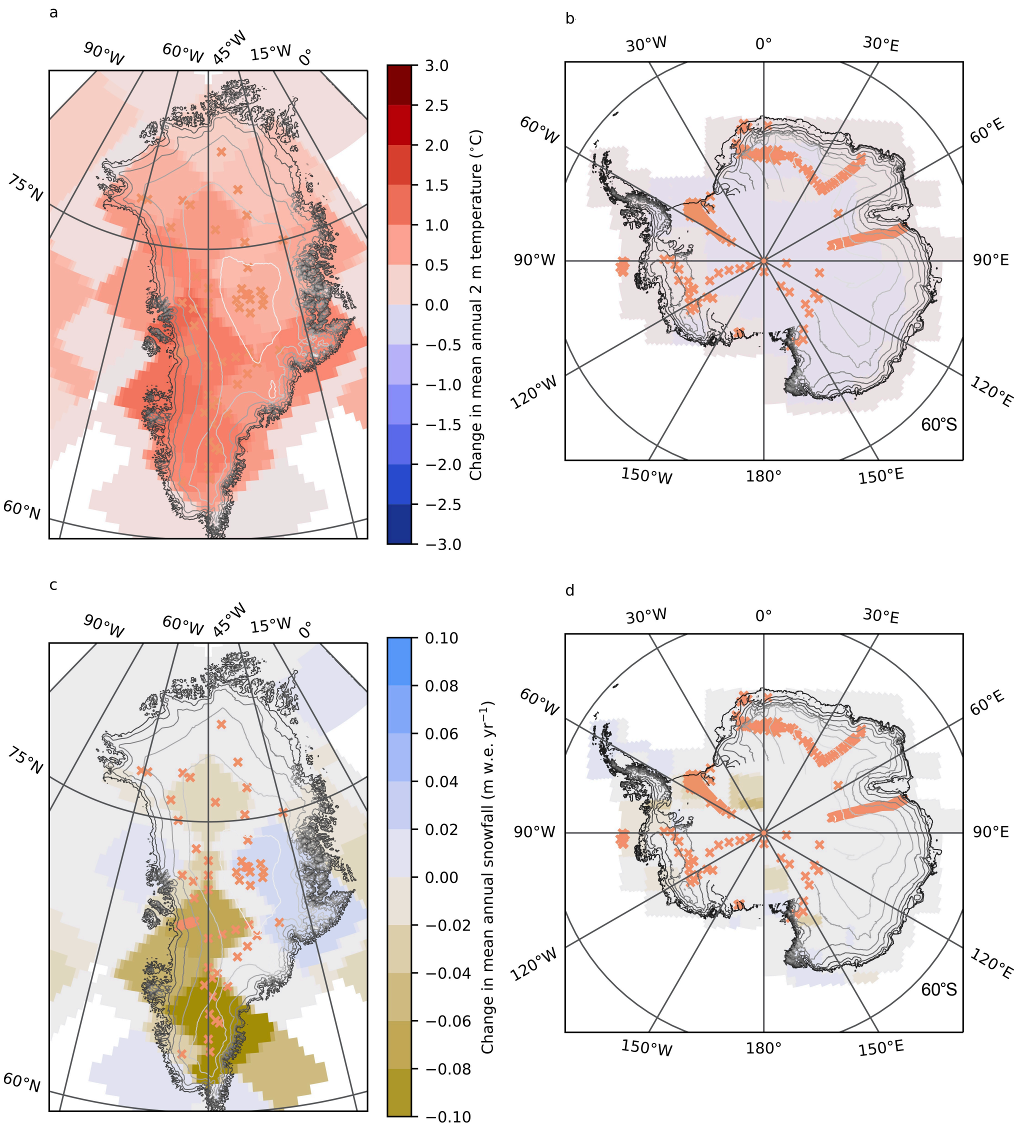

Figure 2. Greenland (a, c) and Antarctica (b, d) 1921–2000 climate change (from CRUNCEP) relative to 1901–1920 (Fig. 1) in ELM simulations. Also shown are locations of SUMup density measurements (Montgomery et al., 2018) used in this study, which range in time from 1980 to 2010. As in Fig. 1, maps shown use the Lambert azimuthal equal-area projection, have different scales, and include elevation contours at 500 m intervals that are generated using data from Howat et al. (2014) (for Greenland) and from Bamber et al. (2009) (for Antarctica).

AIS extending deeper than our simulated snowpacks, RMSE there are calculated only for depths down to 60 m. Some measurements from the GrIS are limited to the near surface of the snowpack, which also limits the depth of RMSE (i.e., measured densities are not extrapolated in depth for the sake of evaluation). This evaluation of ELM-simulated versus observed snowpack characteristics is presented for the three different dynamic firn density parameterizations discussed in detail in Section 3.1.

3.3.3 Firn air content (FAC)

To evaluate how A10, vK17, and vK17+ capture the depth-integrated (rather than depth-local) realism of the simulated versus observed firn, upper 10 m and upper 60 m firn air content (FAC_{10} and FAC_{60}, respectively) in ELM experiments was calculated and compared with the empirical (linear regression) FAC_{10} model from Vandecrux et al. (2019) (as defined in their eq. (1) and eq. (2)). The empirical model of Vandecrux et al. (2019) (V19) is valid for the GrIS dry snow zone over the time period 1953–2017 where the long term mean temperature is within -30° to -19°C. RMS differences (RMSD) between ELM results and V19 were calculated for ELM grid-cells with at least 10 m of firn (depth, not SWE) during the simulation time period of 1953–1970 and for mean annual temperatures of -30° to -19°C. As before, ELM results assessed here stop after 1970 to include more dry snow gridcells that otherwise reach snowpack temperatures greater than 273.12 K, which disqualifies a gridcell entirely from the evaluation. We note here that there is no explicit geographical restriction for ELM results included in these calculations, so RMSD include values from outside of Greenland if they fall within the mean annual temperature domain of -30° to -19°C and have snowpack temperatures that never exceed 273.12 K.

4 Results

To disentangle model and observational differences resulting from atmospheric reanalysis (i.e., the temperature and precipitation forcing) from those caused by snowpack and firn densification model limitations, first we control for mean annual temperature ($\bar{T}$) and accumulation rate (A) and compare (quasi-) steady-state density profiles in ELM simulations in regions representative of dry-snow zones (-37°C $< \bar{T} <$ -19°C and $A <$ 0.5 m SWE yr^{-1}) to the empirical model of HL80. Considering dry snow only (i.e., where snowpack temperatures never exceed 273.12 K), the 16 layer, two-stage density parameterization in ELM (A10) results in densities that agree best with the empirical model of HL80 in the 20 to 60 m depth interval (Fig. 3). However, discrepancies versus HL80 in the 0 to 10 m interval are larger in A10 ($\sim$70 kg m^{-3}) than in results from the 12 layer CLM5 (vK17) and the 16 layer vK17+ density parameterizations. With respect to HL80, the vK17 and vK17+ ELM configurations both demonstrate realistic near surface (upper 10 m) densification except possibly where $\bar{T} >$ -25°C. In these relatively warm regions, simulated upper 10 m densities can be positively biased (too dense) within the 3 to 6 m depth interval. Deeper than 20 m, the A10 experiment agrees better with HL80 compared to the vK17 experiment, which asymptotically stagnates at 550 to 600 kg m^{-3} depending on the temperature. This stagnation in vK17 results in density discrepancies (up to 180 kg m^{-3} in Fig. 3f) compared to HL80 for depths greater than 25 m. These discrepancies indicate a negative bias (densities too low) in the vK17 experiment that exist for all mean annual surface temperatures. With 16 layers, the vK17+ experiment, compared to vK17, agrees slightly better with HL80 for $\bar{T} \approx$ -34°C, but it still does not result in intermediate depth (10 to 60 m) densities within the HL80 range. Despite the persistent discrepancies at intermediate depths, densification in the vK17+ does not stagnate, a result possibly indicating more accurate compaction rates than in vK17 deeper than 20 m.

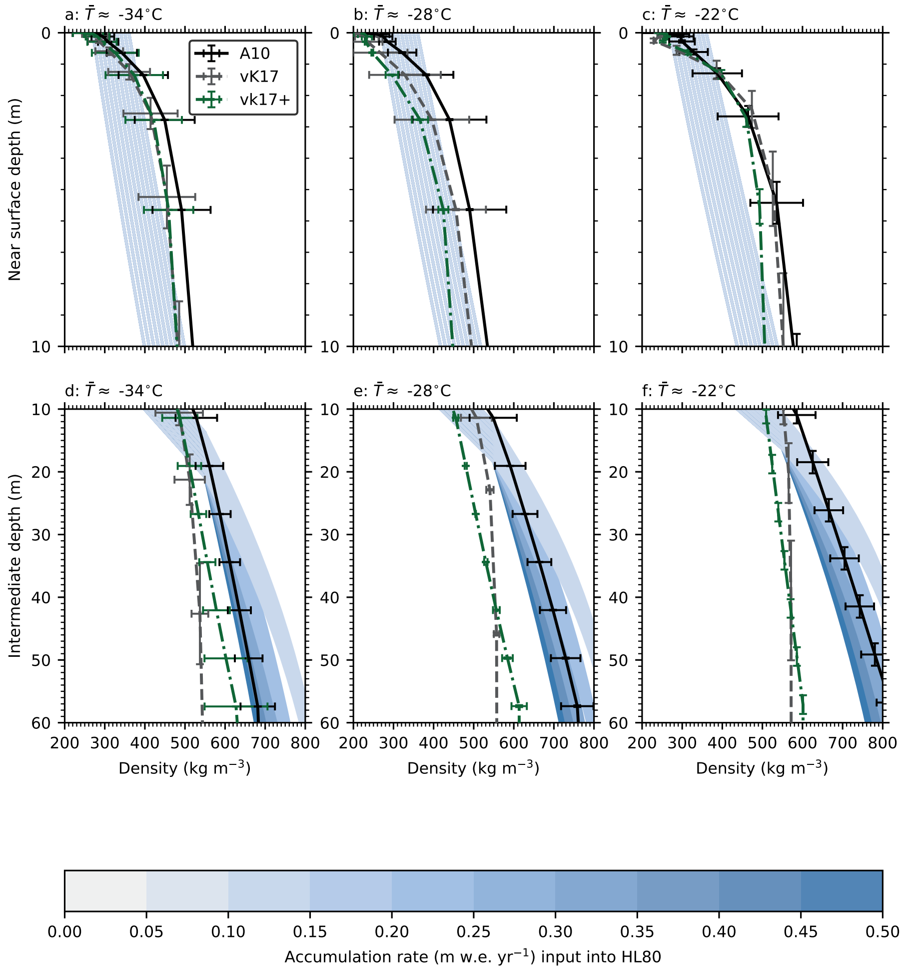

Figure 3. Variation of mean near surface (a, b, and c) and intermediate (d, e, and f) densities with depth in the vK17 (dashed, gray), A10 (solid, black), and vK17+ (dash-dotted, green) ELM experiments compared with those calculated from the model of Herron and Langway (1980) (HL80, light-blue shading) as a function of accumulation rate (colorbar). Note that the HL80 model is independent of accumulation rate above the critical depth (where $\rho < 550$ kg m^{-3}) and that its range overlaps itself. Data are sorted and are graphed by mean annual temperature as indicated by sub-figure titles. ELM results shown represent grid-cells with dry snow only (maximum snowpack temperature < 273.12 K) that are forced with mean annual temperatures within 3°C of -34 (a, d), -28 (b, e), or -22°C (c, f) and with accumulating snowfall not exceeding 0.5 m SWE yr^{-1}. Horizontal error bars show standard deviations indicating spatial variability across grid-cells of twenty year (1901–1920) mean densities represented by reference layers that can vary in depth. Vertical error bars show standard deviations indicating variability of depth across grid-cells for a given reference layer. Note the change in vertical scale from a, b, and c (0 to 10 m), to d, e, and f (10 to 60 m).

Table 3. Mean 1901–2000 Antarctic (1901–1970 Greenland) temperature ($\bar{T}$) and snowfall rate (A) conditions and resulting root-mean-squared-errors (RMSE) evaluated by grid-cell[a] (for dry snow only[b]) in ELM firn density experiments (vK17, vK17+, and A10) with respect to measurements conducted from 1980 to 2010 included in the SUMup dataset (Montgomery et al., 2018).

Nodal coordinates		Climate conditions		RMSE (kg m^{-3})		
Lat. (°N)	Lon. (°E)	$\bar{T}$ (°C)	A (m SWE yr^{-1})	vk17	vk17+	A10
78.2	**-32.2**	**-28**	**0.37**	**149**	**142**	**83**
76.0	**-45.0**	**-30**	**0.48**	**123**	n/a	**46**
74.3	**-39.1**	**-31**	**0.62**	**128**	n/a	**67**
72.6	-34.3	-28	0.74	107	n/a	85
71.3	-40.0	-28	0.79	59	n/a	62
-75.4	**-7.0**	**-49**	**0.38**	**94**	**107**	**123**
-75.4	**7.0**	**-55**	**0.40**	**224**	**211**	**149**
-77.6	**-98.4**	**-30**	**0.38**	**118**	n/a	**34**
-78.2	**-122.2**	**-32**	**0.22**	**158**	**129**	**97**
-78.2	**147.8**	**-45**	**0.29**	**130**	**85**	**101**
-79.2	**-112.1**	**-32**	**0.21**	**146**	**113**	**80**
-79.8	**-100.3**	**-38**	**0.22**	**144**	**116**	**98**
-81.1	135.0	-47	0.15	116	101	130
-82.5	122.7	-53	0.09	107	77	85
-83.4	**-106.0**	**-39**	**0.19**	**167**	**133**	**121**
-83.4	106.0	-56	0.06	111	36	84
-84.2	135.0	-53	0.12	106	139	158
-85.5	-65.9	-35	0.17	37	62	44
-85.5	**-114.1**	**-39**	**0.17**	**112**	**82**	**79**
-85.5	155.9	-50	0.15	137	81	119
-85.5	114.1	-55	0.08	117	81	109
-87.4	**135.0**	**-56**	**0.11**	**96**	**111**	**163**
-87.4	**-135.0**	**-44**	**0.15**	**107**	**74**	**75**

[a]**Bold** indicates a grid-cell where RMSE evaluations extend 60 m in depth.
[b]"n/a" indicates a grid-cell where snowpack temperature exceeds 273.12 K.

To quantify model accuracy, next we examine individual ELM grid-cells and evaluate RMSE in simulated density profiles against a comprehensive collection of in situ firn density measurements (Montgomery et al., 2018) from Greenland and Antarctica. On the GrIS, considering only ELM grid-cells where maximum snow temperature up until 1970 is less than 273.12 K and where available measurements extend to at least 10 m below the surface, we find that RMSE in ELM (northern latitudes reported in Table 3) range from 46 kg m^{-3} (Fig. 4f; A10) to 149 kg m^{-3} (Fig 4c; vK17). Median RMSE is smallest in A10 (67 kg m^{-3}), followed by vK17 (123 kg m^{-3}). Results from the vK17+ experiment are excluded from all but one grid-cell, which indicates that its modifications are more likely to induce melt. Because results from the A10 experiment appear in more grid-cells than both vK17 and vK17+, the A10 configuration is least likely to induce melt. Considering the single GrIS grid-cell for which all three experiments do not experience melt (Fig. 4c), our results indicate that the density profile comparison is similar to the general findings of the steady-state, HL80 evaluation (Fig. 3), which contains the same mean annual temperature (-28°C) and accumulation rate 0.37 m SWE yr^{-1} conditions.

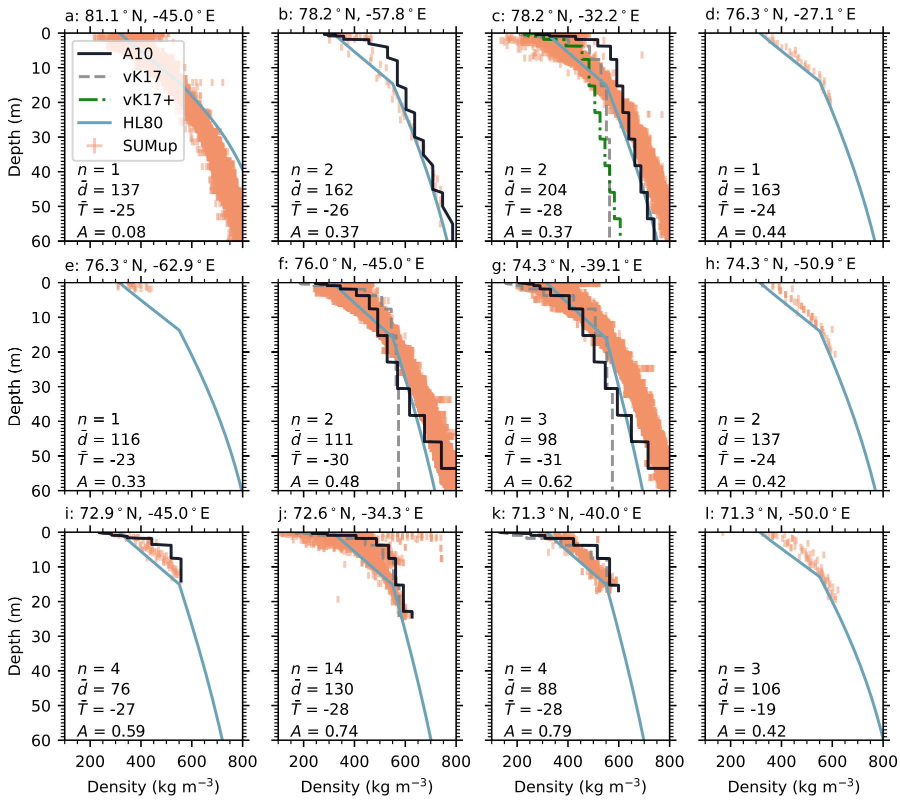

Figure 4. Variation of GrIS density with depth by ELM grid-cell, including only melt free grid-cells that contain locations of available SUMup density measurements (Montgomery et al., 2018). Firn densities simulated in the vK17 (dashed, gray), A10 (solid, black), and vK17+ (dash-dotted, green) experiments are graphed if (and only if) maximum snowpack temperature never exceeded 273.12 K. SUMup density measurements from 1980–2010 (scattered orange crosses) are sorted into groups representing n locations and are graphed by nearest ELM node (indicated by subplot lat-lon coordinates at an average distance $\bar{d}$ [km] away from its accompanying group of measurements) for corresponding geographical comparisons and RMSE calculations. Mean 1901–1970 temperature $\bar{T}$ (°C) and snowfall rate A (m SWE yr^{-1}) are indicated for each ELM grid-cell and are plugged into the empirical model of HL80 (with ρ_0 = 315 kg m^{-3}), which is plotted (solid, light blue) for reference.

On the AIS, we find that intermediate depth (10 to 60 m) densities simulated in all ELM experiments are too small (Fig. 5). Of all the grid-cells containing locations where first, measurements are available between 1980 and 2010, and second, the maximum 1901-2000 snowpack temperature in ELM is less than 273.12 K – adhering to our definition of ELM's dry snow-zone – RMSE (southern latitudes reported in Table 3) range from 34 kg m^{-3} (Fig. 5y; A10) to 224 kg m^{-3} (Fig. S1r; vK17). Median RMSE is smallest in vK17+ (85 kg m^{-3}), followed by A10 (100 kg m^{-3}), then vK17 (117 kg m^{-3}). Despite some evidence of too rapid densification near the GrIS surface in our A10 experiment, colder regions on the AIS result in density profiles that vary too weakly with depth. Negative biases (simulated densities too low) emerge for all three experimental configurations as temperatures decrease. As mean annual temperatures drop below -30°C, densities in the A10 experiment, which are accurate at intermediate-depths (10 to 60 m) for warmer temperatures, diverge from measurements and approach results from the vK17 and vK17+ experiments. In very cold regions ($\bar{T}$ < -40°C), densities in the vK17+ experiment vary more strongly with the long-term accumulation rate than in vK17 and in A10. This enhanced sensitivity is apparent for accumulation rates less than 0.2 m SWE yr^{-1}.

To assess FAC$_{10}$ in ELM experiments, we evaluate RMSD against the empirical model of V19, which accurately predicts FAC$_{10}$ to within 0.4 m across the GrIS dry-snow zone given a particular location's long term mean surface temperature ($\bar{T}$) (Vandecrux et al., 2019). These results suggest that the vK17 and vK17+ firn density parameterizations more accurately simulate near-surface (upper 10 m) densification compared to the A10 (Fig. 6). For -30°C < $\bar{T}$ < -25°C, FAC$_{10}$ distributions in vK17 and vK17+ experiments are relatively close (RMSD of 0.7 m) to the mean observed value of 5.2 (± 0.3) m for the GrIS dry snow zone. In A10, however, FAC$_{10}$ is biased low (not enough pore space), and there exists considerable variability resulting in the relatively large RMSD of 1 m (19%).

To examine how FAC deeper than 10 m varies across ELM experiments, we integrate FAC from 0 to 60 m and, as with FAC$_{10}$, evaluate results as a function of the long term (1953–2000) mean temperature and snowfall rate inherent from the surface boundary conditions. We find that the greater temperature sensitivity of the two-stage firn densification model (A10) results in small changes in upper 60 m FAC (FAC$_{60}$) for colder regions ($\bar{T} < -37$°C) but for relatively warm regions a decrease in FAC$_{60}$ of at least 20% (Fig. 5d, e, and f). Results are consistent across the vK17, vK17+, and A10 experiments for regions where mean temperatures are less than -37°C, where FAC$_{60}$ decreases with increasing temperature and ranges from about 37 to 20 m, which is equivalent to a depth-integrated porosity (DIP) of 62 to 33%. For relatively warm regions, however, as mean temperatures increase above -37°C, FAC$_{60}$ is increasingly less in the A10 than in the vK17 and vK17+ experiments. These differences are most apparent for temperatures greater than -31°C, where FAC$_{60}$ in the vK17 and vK17+ experiments generally range between 21 m and 29 m (35 to 48% DIP) while FAC$_{60}$ in A10 ranges from about 15 to 22 m (25 to 37% DIP).

5 Discussion

This paper describes a 16 layer, two-stage firn density parameterization (A10) in an Earth system model (ELM) that better accommodates dry firn densities deeper than 20 m. We demonstrate that discrepancies between densities in the vK17 experiment and in empirical data, including those from the HL80 model and from the (1980–2010) SUMup measurements, increase with depth and are as large as 180 kg m^{-3} at 60 m. In ELM grid-cells where geographic RMSE evaluations extend as deep as 60 m (bold values in Table 3), a paired difference t-test indicates that the average RMSE decrease of 41 kg m^{-3} (31%) in A10 versus vK17 is significant (p-value < 0.01). Switching from the vK17 to the A10 configuration also significantly decreases RMSE by an average of 22 kg m^{-3}

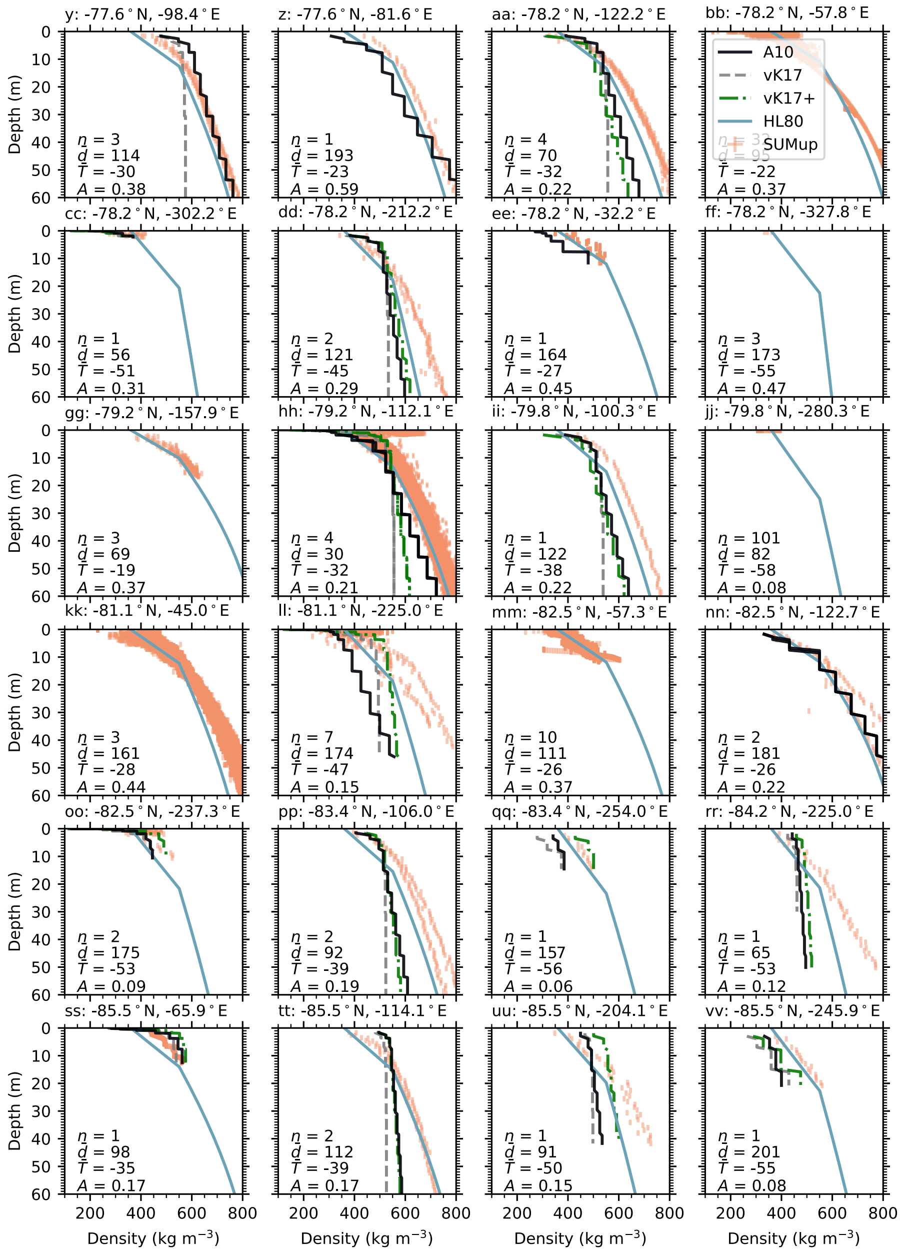

Figure 5. Variation of AIS density with depth by ELM grid-cell, including only melt free grid-cells that contain locations of available SUMup density measurements (Montgomery et al., 2018). Firn densities simulated in the vK17 (dashed, gray), A10 (solid, black), and vK17+ (dash-dotted, green) experiments are graphed if (and only if) maximum snowpack temperature never exceeded 273.12 K. SUMup density measurements from 1980–2010 (scattered orange crosses) are sorted into groups representing n locations and are graphed by nearest ELM node (indicated by subplot lat-lon coordinates at an average distance $\bar{d}$ [km] away from its accompanying group of measurements) for corresponding geographical comparisons and RMSE calculations. Mean 1901–2000 temperature $\bar{T}$ (°C) and snowfall rate A (m SWE yr^{-1}) are indicated for each ELM grid-cell and are plugged into the empirical model of HL80 (with ρ_0 = 360 kg m^{-3}), which is plotted (solid, light blue) for reference. The full figure, which shows comprehensive results from 50 grid-cells labeled a, b, . . . , y, z, aa, bb, . . . , ww, xx, is provided as a supplement.

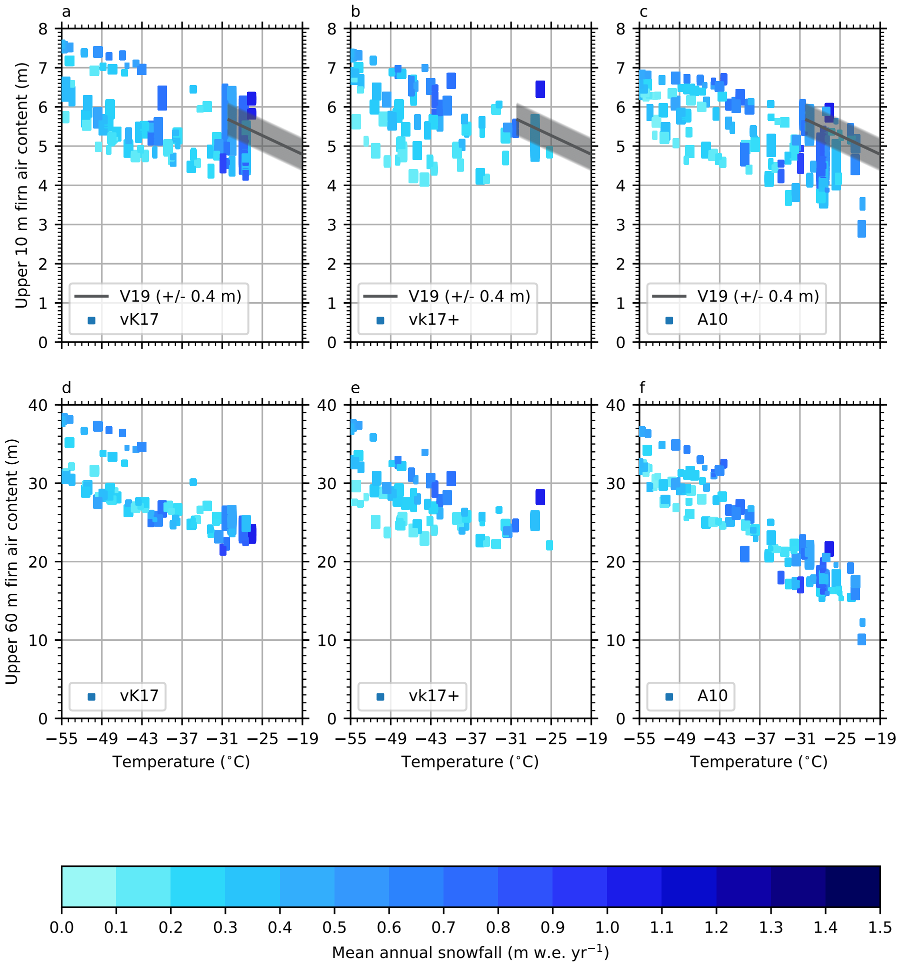

Figure 6. Depth-integrated firn air content in the upper 10 m (FAC_{10}; a, b, c) and in the upper 60 m (d, e, f) for the vK17 (a, d), vK17+ (b, e), and A10 (c, f) ELM experiments. FAC is plotted as a function of mean 1953–2000 2 m air temperature and is compared with the empirical FAC_{10} model of Vandecrux et al. (2019) (V19) where valid. ELM values correspond to the range of interannual snapshots (from 1953 to 2000) from individual grid-cells where maximum snowpack temperatures are less than 273.12 K with corresponding mean annual snowfall rates represented by the colorbar. The uncertainty range of the empirical model (± 0.4 m) is indicated by gray bands above and below the best fit line from which ELM RMS deviation (RMSD) is calculated over the temperature range of -30° to -19°C. Accordingly, RMSD are 0.71 m for vK17 (a), 0.70 m for vK17+ (b), and 1.01 m for A10 (c).

(19%; p-value = 0.03) in all grid-cells regardless of the vertical extent of their evaluations. These results reject the null hypothesis that density errors (at depths of 0 to 60 m) are the same in the vK17 and A10 experiments. Compared to vK17 and vK17+, which underestimate 10 to 60 m dry firn densities in all but just two or three ELM gridcells, our data show that the A10 configuration results in at least a 20% decrease in FAC_{60} for warm regions ($\bar{T} > -31°C$) of the dry snow zone. Taken together, these findings suggest that the A10 density parameterization will produce better results than the vK17 (or vK17+) configuration for studies that require accurate total FAC in warm dry snow zones (e.g., Greenland's interior ice sheet and Antarctic ice shelves).

The decrease in FAC_{60} in the A10 versus vK17 (and vK17+) experiments vanishes for colder temperatures, where both the density profile and FAC results in A10 approach those of the vK17 and vK17+ experiments. Similar results across the vK17, vK17+, and A10 experiments for cold temperatures that diverge for warmer temperatures indicate a greater temperature sensitivity of the A10 density parameterization. We expect this divergent behavior for warm temperatures because the underlying compaction model, given in eq. (8), was originally calibrated using measurements of strain rates in the upper 20 m, the upper 10 m of which is subject to seasonal fluctuations in temperature (Arthern et al., 2010). Therefore, the A10 parameterization captures temperature driven processes without accounting for the more steady, background compaction rates that dominate at greater depths and colder climates. On the other hand, because of its weaker temperature dependence and lack of snow grain size dependence, the vK17 configuration produces the most consistent density profiles for various climate conditions and across multiple ELM grid-cells. In addition to adding layers, an attempt at tuning the vK17 parameterization in a vK17+ configuration lead to insignificant differences despite the improved vertical resolution. This finding rejects the hypothesis that the spatial correlation (geographically) of densities versus depths can be improved by calibrating the overburden pressure compaction coefficients, which partially modulate the temperature sensitivity. Furthermore, it is unlikely that increasing the vertical resolution (i.e., from 12 to 16 layers) will significantly improve the vK17 density parameterization at intermediate depths, a finding supported by results from Stevens et al. (2020), where the negative bias (densities too low) exists despite having a higher resolution vertical grid. In theory, colder parts of the dry snow zones will be the last to experience melt under future warming scenarios, so too much FAC resulting from the vK17 and vK17+ density parameterizations is most problematic for climatic mass balance studies at the dry-snow-zone threshold (i.e., where the melt extent is expanding).

Our results confirm that the vK17 firn density parameteriztation does not adequately represent the second stage of densification, i.e., where densities exceed 550 kg m^{-3}. While CLM5 (Lawrence et al., 2019) includes substantial improvements that eliminate biases in ice sheet surface densities and the critical depths where densities reach 550 kg m^{-3}, there is no guarantee of accuracy for densities in the second stage. Nevertheless, only after implementing the developments of van Kampenhout et al. (2017) are we able to pick up the study in ELM, where we first, better resolve the densification at intermediate depths by using a 16 layer vertical grid appropriate for modeling both a shallow ($\sim$1 m) seasonal snowpack and deeper ($\sim$60 m) perennial firn, and second, test new firn density parameterizations that compensate FAC_{10} errors with more accurate densities at depths greater than 20 m. Because firn density profiles are dependent on the microphysical properties of the snowpack structure (Montagnat et al., 2020), our findings do not imply that any particular configuration will strengthen the spatial correlation between measured and simulated densities. They do, however, suggest that the improved density profile of A10 for depths greater than 20 m likely results in a more realistic total FAC than in vK17, the default firn density parameterization in CLM5. This result is particularly desirable for regions where surface melt, percolation, and refreezing extend deep below the surface.

Alternatively, a hybrid vK17 (first stage) / A10 (second stage) density parameterization could potentially provide a model that maintains the accurate critical depths of vK17 with more accurate FAC_{60} resulting from faster densification of A10 for higher densities. Before adopting this approach, however, it should be tested to further evaluate the possibility of the second stage in A10 compensating compaction rates that are too low at depth with compaction rates that are too high near the surface. Such an outcome would suggest that the A10 experiment only results in more realistic intermediate densities because of near-surface densification that is too fast. A similar compensating bias exists in the original, CLM4 snow density parameterization (from Anderson, 1976), which van Kampenhout et al. (2017) resolve by replacing the overburden compaction eq. (2) with eq. (4) (from Vionnet et al., 2012). We also speculate that modifying ELM's original dynamic viscosity parameterization, given in eq. (2), can better accommodate compaction rates more typical of firn by increasing the coefficient η_0 by a factor of about 50. This simple adjustment is possible because the dynamic viscosity η from eq. (2) versus eq. (4) have essentially the same functional form, though with slightly different coefficients. Testing these iterative developments – described above and in A10+ configurations – in further ELM simulations and evaluating their impacts on ice sheet climatic mass balance is left for a follow-on study.

Despite having consistent surface temperature and snowfall conditions, there are 39 and 78% more dry snow ELM gridcells in A10 than in the vK17 and vK17+ experiments, respectively. This unexpected result indicates that the top (2 cm) layer of the snowpack with the A10 density parameterization is more resilient to warm surface temperatures than with the vK17 and vK17+ experiments. Because of higher near-surface densities for warm grid cells in A10, increased conduction via a higher thermal conductivity causes a more rapid downward transfer of energy, thus allowing top layer temperatures to stay cooler than under the same conditions in the vK17 and vK17+ experiments. This conjecture explains why fewer data appear in Figs. 4, 5, and 6 for vK17 and vK17+, where there exist more gridcells where snowpack temperatures reach 0°C, than for A10.

Because we generalize the application of HL80 by using an analytical expression forced by a matrix of climate conditions, our steady-state analysis (Fig. 3) has the disadvantage of not offering evaluations that are specific for a particular location. However, by forcing HL80 with a matrix spanning plausible climate conditions combined with an array of surface densities encompassing measurements, we generate a range of empirical density profiles that are independent of biases in ELM's atmospheric forcing data. By comparing ELM mean densities and standard deviations by snowpack layer with the range of densities from our HL80 implementation, we examine where biases are large and significant as a function of firn depth, mean annual temperature and snowfall rate. It is also important to consider that given the ELM climate conditions, the analytic form of HL80 fails to track through the center of SUMup density measurements within each particular grid-cell. This empirical mismatch, between measurements and HL80, indicates that our methodology is imperfect. The imperfections arise primarily from a coarse horizontal resolution that results in"bulk weather," which can misrepresent the true climate conditions for a relatively small region around a set of local measurements encompassed by a larger ELM grid-cell. Furthermore, the precision of HL80 is limited by a relatively large uncertainty in its accumulation rate parameters (Verjans et al., 2020). Despite these limitations, when given the coarse resolution climate conditions in ELM and empirical surface densities, HL80 generally results in better agreement with measurements than that of the ELM experiments. Therefore, using HL80 as a standard to evaluate against for this study is sufficient while the state of firn in Earth system models remains one-dimensional and unphysical (i.e., highly parameterized). For example, although the A10 parameterization improves intermediate densification compared to vK17, its implementation into ELM does not represent a complete, process-based thermomechanical model that includes all drivers of snow compaction. With simple parameterizations of bulk densification due to gravitational settling and accretion of snow grains, sublimation, and other relevant processes, modeling deficiencies near the surface arise, especially where densities range from 300 to 500 kg m^{-3} and vary due to sub-grid scale snow microstructure properties not accounted for in one-dimensional firn models (Lundin et al., 2017).

Further complicating the challenge is that in the Community Firn Model framework (Stevens et al., 2020), most of the participating (individual) firn densification models use a mean mass accumulation rate as a proxy for overburden stress, while those that call for overburden stress explicitly are given expressions of accumulation rates and age instead of the depth integrated overburden stress itself. The depth integrated overburden load (i.e., the columnar mass density σ), a state variable, can be calculated directly and is preferred in an Earth system model, for which accumulation rates (and other mass and energy exchanges at the surface) vary on sub-daily timescales. As far as we know, this is the first study that tests the stress-based formulation of the semi-empirical firn densification model of Arthern et al. (2010). Previous studies use the "semi-empirical" model in idealized experiments (Kuipers Munneke et al., 2015; Ligtenberg et al., 2011), but we are aware of none that calculate the overburden pressure or grain load stress as an input to the model. Furthermore, this study is the first that couples the model of Arthern et al. (2010) with an Earth system model's snow metamorphism routine. Like in CLM, ELM uses the snow grain size evolution routine of Flanner and Zender (2006), which is closely linked to the SNICAR model via its snow grain size parameter r_e. Including the dynamic snow grain size parameter in the snow compaction equation, new metamorphic feedbacks are possible. The disadvantage of this new link is that it adds complexity to the model. So while it has the potential to improve the spatial correlation of results with observations, the added complexity also brings difficulty in disentangling confounding factors to support plausible explanations for simulated phenomena. It remains to be determined whether this trade-off will be worthwhile. To address this question, future studies will vary initial r_e to further examine its impact on the process of firn densification and, more broadly, the complexities of ice sheet surface to atmospheric coupling.

Incorporating snow grain size dependence into snow and firn compaction equations in conjunction with variable initial snow grain size could improve the spatial correlation between observed and modeled total FAC. Perhaps an initial modification would be to add a temperature dependence to initial snow grain size (as carried out by van Kampenhout et al., 2020). Another option is to add a moisture-content dependence, which is motivated by the fact that ice crystal shape habit in the atmosphere is closely related to the specific humidity (Libbrecht, 2005). By varying the initial snow grain radius as a function of humidity, where grain size increases with decreasing humidity, the compaction model could be indirectly linked to the accumulation rate. This link, which in ELM currently relies only on the depth-integrated snow overburden pressure, would help stabilize systematic compaction rate biases that seem to vary with the local accumulation rate. While most of our model grid cells have relatively high accumulation rates, the few that are below 0.2 m SWE yr^{-1} demonstrate densities that vary too quickly in depth. In high accumulation areas, the downward advection relative to the surface that a parcel of snow experiences is fast. Burial of near surface snow by new, relatively low density snow causes the near surface layers to increase in depth rapidly, without having time for integrated compaction rates to allow the model density profile to track that seen in measurements. In low accumulation areas, a parcel of snow near the surface stays near the surface for longer, which allows enough time for the integrated compaction rates to cause model densities to surpass measurements. This indirect accumulation rate sensitivity is most apparent in the vK17+ experiment. By further indirectly linking a firn densification model to the local accumulation rate via a specific humidity dependence of the initial snow grain size, an Earth system model could possibly mitigate systematic density errors while also correcting albedo biases inherent from oversimplifying ice crystal morphology.

Ultimately, this study will enable better predictions of sea level rise as a direct result of GrIS surface melt and mass loss. Fortunately, Earth system models, while offering the advantage of globally consistent physics needed for global mean sea level rise projections, can accommodate simulating firn densification in relatively warm dry snow zones by expanding their snowpack modules' layering schemes and implementing two-stage firn densification models (e.g., the A10 parameterization presented in this study). On the other hand, accurately simulating ice sheet climatic mass balance still requires a higher horizontal resolution (Noël et al., 2018), and modeling densification in the presence of liquid water is difficult where parameterizations remain untested and ill-constrained (Verjans et al., 2019). Consequently, accurate partitioning of the climatic mass balance terms remains a challenge in Earth system modeling. Although regional climate models enable a higher spatial resolution, limitations in our understanding of supra-glacial hydrology still remain a source of uncertainty in determining Greenland's future contribution to sea level rise (Fettweis et al., 2020). To address these uncertainties, future developments will seek to improve the capability of simulating supra-glacial hydrology in E3SM, including better quantifying surface melt, percolation, refreezing, and the build-up of perennial aquifers (Miège et al., 2016; Forster et al., 2014; Koenig et al., 2014; Munneke et al., 2014). For now, the new ELM firn capability presented here allows future studies to initialize the GrIS snowpack and firn conditions in the fully coupled E3SM with the specific goal of improving its simulated climatic mass balance. Applied globally, this capability also better prepares E3SM for studying perennial snow cover and related albedo feedbacks affecting Earth's climate.

6 Conclusions

As part of a larger effort to introduce dynamic ice sheets in E3SM, this study incorporates into ELM approximations applied in firn densification models and demonstrates the new Earth system modeling capability of accommodating a total firn thickness of up to 60 m. We compared simulations from three competing implementations of these process-based models in ELM (i.e., vK17 vK17+, and A10) against available observations from cold, dry firn cores in both hemispheres. Overall, our findings highlight the firn density parameterizations' differences associated with their ability to reproduce the steady-state density profiles calculated from the empirical model of HL80 and measurements from the Greenland and Antarctic ice sheet dry snow zones. Despite the successful representation of densification above the critical depth, the formulation employed by CLM5 (vK17) yields unrealistic densification below the critical depth, where the processes involved warrant a new approach. To improve densities below the critical depth, we replaced the vK17 overburden compaction equation with a two-stage, semi-empirical formulation (A10). Considering only the ELM grid-cells that encompass SUMup density measurements extending at least 60 m in depth, switching from the vK17 to the A10 density parameterization resulted in an average RMSE decrease of 41 kg m^{-3} (31%), which emphasized significant improvement for intermediate (20 to 60 m) depths. Finally, relative to the vK17 and vK17+ experiments, the A10 density parameterization decreased FAC$_{60}$ by at least 20% in warmer ($\bar{T} > -31$°C) dry snow zones, leading to the conclusion that its two-stage overburden compaction formulation should be used in studies that require an accurate total FAC.

Appendix A Statistical model and optimization of vK17(+)

To simulate a statistical model of the dry snow zones across Antarctica and Greenland, NumPy's random number routines are used to generate n (10^4) pseudo-random surface bulk densities ($\bar{\rho_0}$), mean annual temperatures ($\bar{T}$), and accumulation rates (A) representative of ice sheets. Considering that $\bar{\rho_0}$ approximates the mean of a large number of surface density samples independent and identically distributed over a relatively large region (> 1 km^2), the probably distribution function (PDF) $f(\bar{\rho_0})$ is assumed to be normal (Gaussian), expressed as

$$f(\bar{\rho_0}) = \frac{1}{s\sqrt{2\pi}} \exp\left\{-\frac{1}{2s^2}(\bar{\rho_0} - \mu)^2\right\}, \tag{A1}$$

with mean $\mu = 340$ kg m^{-3} and standard deviation $s = 20$ kg m^{-3}. Similarly, random mean-annual temperatures $\bar{T} <$ -25° C were drawn from the left tail of a Gaussian distribution (with an estimated global mean $\mu = 14.9°$ C and standard deviation = 16° C) selected to give a distribution of temperatures crudely representative of Earth's cold land surface. Deeper than 10 m, snowpack temperatures $T(z)$ are assumed equal to the annual mean $\bar{T}$, but upper 10 m temperatures are randomized as follows. First, a random surface temperature T_0 [K] is drawn using the PDF from eq. (A1), but with $\mu = \bar{T}$ and $s = 8$ K. Second, $T(z)$ [K] is calculated from

$$T(z) = \bar{T} - \frac{T_0(z - z_{10})^3}{\nu}, \tag{A2}$$

with $\bar{T}$ and T_0 in (units of) K, $z_{10} = 10$ m, and $\nu = 1000$ m^3. Mean accumulation rates (A) are drawn at random from a lognormal distribution selected to give values representative of relatively warm ($\bar{T} >$ -51° C) or cold ($\bar{T} \leq$ -51° C) dry snow zones, with 0.07 $< A <$ 0.4 or $A <$ 0.07 m SWE yr^{-1}, respectively (Herron & Langway, 1980). Valid mean annual temperature and accumulation rate pairs are then combined with independent surface densities and are inserted into the empirical model of HL80. In this manner, n plausible density versus depth relationships are generated, from which we approximate empirical steady-state strain rates (with a vertical resolution of 10 cm) using eq. (7). Finally, the sum of squared residuals between empirical strain rates and those predicted by the vK17 parameterization, given the same density (and overburden pressure) profiles but with $T(z)$ from eq. (A2), are minimized using a least squares regression algorithm. This regression algorithm, which includes an additional constant (c_6) from the design matrix, is used to optimize the coefficients c_3, from eq. (3), and f_2, from eq. (4).

Acknowledgments

The E3SM (version 1.2.0) source code is maintained by the E3SM Project, which is available at `https://doi.org/10.11578/E3SM/dc.20210308.1` and is sponsored by the U.S. Department of Energy, Office of Science, Office of Biological and Environmental Research. E3SM source code modifications and development that will reproduce these results are available from Edwards et al. (2020). ELM simulation data, associated python analysis scripts, and the offline statistical firn model referenced in this manuscript are archived and publicly accessible from Schneider (2020). The CLM5 source code is maintained by the CTSM Development Team and is available at `https://doi.org/10.5281/zenodo.3779821`. The extensive SUMup density measurement dataset (Montgomery et al., 2018) is available at `https://arcticdata.io/catalog/view/urn%3Auuid%3A00d2e142-228e-4722-8f12-d054606e3869`. This work is supported by the U.S. Department of Energy's Scientific Discovery Through Advanced Computing (LANL-520117) and Earth System Model Development (DE-SC0019278) programs and used resources of the National Energy Research Scientific Computing Center (NERSC), a U.S. Department of Energy Office of Science User Facility. We are unaware of any conflicts of interest regarding the publication of this manuscript. We are grateful to all the scientists, software engineers, and administrators who contributed to the development of E3SM. We also thank those working on the Community Earth System Model and netCDF software developed by UCAR/Unidata (Rew et al., 1989). Finally, we thank Brooke Medley and an anonymous reviewer for their thoughtful comments and suggestions, which helped us refine our methods, clarify our results and improve the readability of our manuscript.

References

Alley, R. B. (1987). Firn densification by grain-boundary sliding : A first model.

J. Phys. Colloques, *48*, C1-249-C1-256. Retrieved from https://doi.org/10.1051/jphyscol:1987135 doi: 10.1051/jphyscol:1987135

Anderson, E. A. (1976). A point energy and mass balance model of a snow cover. Retrieved from https://repository.library.noaa.gov/view/noaa/6392 (Place: Office of Hydrology, National Weather Service)

Arthern, R. J., Vaughan, D. G., Rankin, A. M., Mulvaney, R., & Thomas, E. R. (2010). In situ measurements of antarctic snow compaction compared with predictions of models. *Journal of Geophysical Research: Earth Surface*, *115*(F3). Retrieved from https://agupubs.onlinelibrary.wiley.com/doi/abs/10.1029/2009JF001306 doi: https://doi.org/10.1029/2009JF001306

Bader, H. (1954). Sorge's law of densification of snow on high polar glaciers. *Journal of Glaciology*, *2*(15), 319–323. doi: 10.3189/S0022143000025144

Bamber, J., Gomez-Dans, J., & Griggs, J. (2009). *Antarctic 1 km Digital Elevation Model (DEM) from Combined ERS-1 Radar and ICESat Laser Satellite Altimetry, Version 1.* NASA National Snow and Ice Data Center DAAC. Retrieved 2021-03-06, from http://nsidc.org/data/NSIDC-0422/versions/1 (type: dataset) doi: 10.5067/H0FQ1KL9NEKM

Cuffey, K., & Paterson, W. S. B. (2010). *The physics of glaciers* (4th ed ed.). Burlington, MA: Butterworth-Heinemann/Elsevier. (OCLC: ocn488732494)

Edwards, J., Foucar, J., Mametjanov, A., Jacob, R., Taylor, M., Singhbalwinder, . . . Hannah, W. (2020, July). *amschne/E3SM: Optimized firn densification in ELM.* Zenodo. Retrieved 2020-07-23, from https://zenodo.org/record/3955331 doi: 10.5281/ZENODO.3955331

Fausto, R. S., Box, J. E., Vandecrux, B., van As, D., Steffen, K., MacFerrin, M. J., . . . Braithwaite, R. J. (2018). A Snow Density Dataset for Improving Surface Boundary Conditions in Greenland Ice Sheet Firn Modeling. *Frontiers in Earth Science*, *6*, 51. Retrieved from https://www.frontiersin.org/article/10.3389/feart.2018.00051 doi: 10.3389/feart.2018.00051

Fettweis, X., Box, J. E., Agosta, C., Amory, C., Kittel, C., Lang, C., . . . Gallée, H. (2017). Reconstructions of the 1900–2015 greenland ice sheet surface mass balance using the regional climate mar model. *The Cryosphere*, *11*(2), 1015–1033. Retrieved from https://tc.copernicus.org/articles/11/1015/2017/ doi: 10.5194/tc-11-1015-2017

Fettweis, X., Hofer, S., Krebs-Kanzow, U., Amory, C., Aoki, T., Berends, C. J., . . . Zolles, T. (2020). Grsmbmip: intercomparison of the modelled 1980–2012 surface mass balance over the greenland ice sheet. *The Cryosphere*, *14*(11), 3935–3958. Retrieved from https://tc.copernicus.org/articles/14/3935/2020/ doi: 10.5194/tc-14-3935-2020

Flanner, M. G., & Zender, C. S. (2006). Linking snowpack microphysics and albedo evolution. *Journal of Geophysical Research: Atmospheres*, *111*(D12). Retrieved from https://agupubs.onlinelibrary.wiley.com/doi/abs/10.1029/2005JD006834 doi: https://doi.org/10.1029/2005JD006834

Flanner, M. G., Zender, C. S., Randerson, J. T., & Rasch, P. J. (2007). Present-day climate forcing and response from black carbon in snow. *Journal of Geophysical Research: Atmospheres*, *112*(D11). Retrieved from https://agupubs.onlinelibrary.wiley.com/doi/abs/10.1029/2006JD008003 doi: https://doi.org/10.1029/2006JD008003

Forster, R. R., Box, J. E., van den Broeke, M. R., Miège, C., Burgess, E. W., van Angelen, J. H., . . . McConnell, J. R. (2014, February). Extensive liquid meltwater storage in firn within the Greenland ice sheet. *Nature Geoscience*, *7*(2), 95–98. Retrieved from https://doi.org/10.1038/ngeo2043 doi: 10.1038/ngeo2043

Fyke, J., Sergienko, O., Löfverström, M., Price, S., & Lenaerts, J. T. M. (2018). An overview of interactions and feedbacks between ice sheets and the earth system. *Reviews of Geophysics*, *56*(2), 361-408. Retrieved from https://

agupubs.onlinelibrary.wiley.com/doi/abs/10.1029/2018RG000600 doi: https://doi.org/10.1029/2018RG000600

Golaz, J.-C., Caldwell, P. M., Van Roekel, L. P., Petersen, M. R., Tang, Q., Wolfe, J. D., ... Zhu, Q. (2019). The doe e3sm coupled model version 1: Overview and evaluation at standard resolution. *Journal of Advances in Modeling Earth Systems*, *11*(7), 2089-2129. Retrieved from https://agupubs.onlinelibrary.wiley.com/doi/abs/10.1029/2018MS001603 doi: https://doi.org/10.1029/2018MS001603

Hagenmuller, P., Chambon, G., & Naaim, M. (2015). Microstructure-based modeling of snow mechanics: a discrete element approach. *The Cryosphere*, *9*(5), 1969–1982. Retrieved from https://tc.copernicus.org/articles/9/1969/2015/ doi: 10.5194/tc-9-1969-2015

Herron, M. M., & Langway, C. C. (1980). Firn densification: An empirical model. *Journal of Glaciology*, *25*(93), 373–385. doi: 10.3189/S0022143000015239

Howat, I. M., Negrete, A., & Smith, B. E. (2014). The greenland ice mapping project (gimp) land classification and surface elevation data sets. *The Cryosphere*, *8*(4), 1509–1518. Retrieved from https://tc.copernicus.org/articles/8/1509/2014/ doi: 10.5194/tc-8-1509-2014

Jordan, R. E. (1991, October). *A One-dimensional temperature model for a snow cover : technical documentation for SNTHERM.89.* Cold Regions Research and Engineering Laboratory (U.S.) / Engineer Research and Development Center (U.S.). Retrieved from http://hdl.handle.net/11681/11677

Koenig, L. S., Miège, C., Forster, R. R., & Brucker, L. (2014). Initial in situ measurements of perennial meltwater storage in the greenland firn aquifer. *Geophysical Research Letters*, *41*(1), 81-85. Retrieved from https://agupubs.onlinelibrary.wiley.com/doi/abs/10.1002/2013GL058083 doi: https://doi.org/10.1002/2013GL058083

Krinner, G., Derksen, C., Essery, R., Flanner, M., Hagemann, S., Clark, M., ... Zhu, D. (2018). Esm-snowmip: assessing snow models and quantifying snow-related climate feedbacks. *Geoscientific Model Development*, *11*(12), 5027–5049. Retrieved from https://gmd.copernicus.org/articles/11/5027/2018/ doi: 10.5194/gmd-11-5027-2018

Kuipers Munneke, P., Ligtenberg, S. R. M., Noël, B. P. Y., Howat, I. M., Box, J. E., Mosley-Thompson, E., ... van den Broeke, M. R. (2015). Elevation change of the greenland ice sheet due to surface mass balance and firn processes, 1960–2014. *The Cryosphere*, *9*(6), 2009–2025. Retrieved from https://tc.copernicus.org/articles/9/2009/2015/ doi: 10.5194/tc-9-2009-2015

Lawrence, D. M., Fisher, R. A., Koven, C. D., Oleson, K. W., Swenson, S. C., Bonan, G., ... Zeng, X. (2019). The community land model version 5: Description of new features, benchmarking, and impact of forcing uncertainty. *Journal of Advances in Modeling Earth Systems*, *11*(12), 4245-4287. Retrieved from https://agupubs.onlinelibrary.wiley.com/doi/abs/10.1029/2018MS001583 doi: https://doi.org/10.1029/2018MS001583

Lawrence, D. M., Oleson, K. W., Flanner, M. G., Thornton, P. E., Swenson, S. C., Lawrence, P. J., ... Slater, A. G. (2011). Parameterization improvements and functional and structural advances in version 4 of the community land model. *Journal of Advances in Modeling Earth Systems*, *3*(1). Retrieved from https://agupubs.onlinelibrary.wiley.com/doi/abs/10.1029/2011MS00045 doi: https://doi.org/10.1029/2011MS00045

Lehning, M., Bartelt, P., Brown, B., Fierz, C., & Satyawali, P. (2002). A physical snowpack model for the swiss avalanche warning: Part ii. snow microstructure. *Cold Regions Science and Technology*, *35*(3), 147 - 167. Retrieved from http://www.sciencedirect.com/science/article/pii/S0165232X02000733 doi: https://doi.org/10.1016/S0165-232X(02)00073-3

Lenaerts, J. T. M., Camron, M. D., Wyburn-Powell, C. R., & Kay, J. E. (2020). Present-day and future Greenland Ice Sheet precipitation frequency from CloudSat observations and the Community Earth System Model. *The Cryosphere*, *14*(7), 2253–2265. Retrieved from `https://tc.copernicus.org/articles/14/2253/2020/` doi: 10.5194/tc-14-2253-2020

Lenaerts, J. T. M., Medley, B., van den Broeke, M. R., & Wouters, B. (2019). Observing and modeling ice sheet surface mass balance. *Reviews of Geophysics*, *57*(2), 376-420. Retrieved from `https://agupubs.onlinelibrary.wiley.com/doi/abs/10.1029/2018RG000622` doi: https://doi.org/10.1029/2018RG000622

Libbrecht, K. G. (2005, mar). The physics of snow crystals. *Reports on Progress in Physics*, *68*(4), 855–895. Retrieved from `https://doi.org/10.1088/0034-4885/68/4/r03` doi: 10.1088/0034-4885/68/4/r03

Ligtenberg, S. R. M., Helsen, M. M., & van den Broeke, M. R. (2011). An improved semi-empirical model for the densification of antarctic firn. *The Cryosphere*, *5*(4), 809–819. Retrieved from `https://tc.copernicus.org/articles/5/809/2011/` doi: 10.5194/tc-5-809-2011

Lundin, J. M., Stevens, C. M., Arthern, R., Buizert, C., Orsi, A., Ligtenberg, S. R., ... Waddington, E. D. (2017). Firn model intercomparison experiment (firnmice). *Journal of Glaciology*, *63*(239), 401–422. doi: 10.1017/jog.2016.114

Miège, C., Forster, R. R., Brucker, L., Koenig, L. S., Solomon, D. K., Paden, J. D., ... Gogineni, S. (2016). Spatial extent and temporal variability of greenland firn aquifers detected by ground and airborne radars. *Journal of Geophysical Research: Earth Surface*, *121*(12), 2381-2398. Retrieved from `https://agupubs.onlinelibrary.wiley.com/doi/abs/10.1002/2016JF003869` doi: https://doi.org/10.1002/2016JF003869

Montagnat, M., Löwe, H., Calonne, N., Schneebeli, M., Matzl, M., & Jaggi, M. (2020, September). On the Birth of Structural and Crystallographic Fabric Signals in Polar Snow: A Case Study From the EastGRIP Snowpack. *Frontiers in Earth Science*. Retrieved from `https://hal.archives-ouvertes.fr/hal-03024371` doi: 10.3389/feart.2020.00365

Montgomery, L., Koenig, L., & Alexander, P. (2018). The sumup dataset: compiled measurements of surface mass balance components over ice sheets and sea ice with analysis over greenland. *Earth System Science Data*, *10*(4), 1959–1985. Retrieved from `https://essd.copernicus.org/articles/10/1959/2018/` doi: 10.5194/essd-10-1959-2018

Munneke, P. K., M. Ligtenberg, S. R., van den Broeke, M. R., van Angelen, J. H., & Forster, R. R. (2014). Explaining the presence of perennial liquid water bodies in the firn of the greenland ice sheet. *Geophysical Research Letters*, *41*(2), 476-483. Retrieved from `https://agupubs.onlinelibrary.wiley.com/doi/abs/10.1002/2013GL058389` doi: https://doi.org/10.1002/2013GL058389

Muntjewerf, L., Petrini, M., Vizcaino, M., Ernani da Silva, C., Sellevold, R., Scherrenberg, M. D. W., ... Lofverstrom, M. (2020). Greenland ice sheet contribution to 21st century sea level rise as simulated by the coupled cesm2.1-cism2.1. *Geophysical Research Letters*, *47*(9), e2019GL086836. Retrieved from `https://agupubs.onlinelibrary.wiley.com/doi/abs/10.1029/2019GL086836` (e2019GL086836 10.1029/2019GL086836) doi: https://doi.org/10.1029/2019GL086836

Noël, B., van de Berg, W. J., van Wessem, J. M., van Meijgaard, E., van As, D., Lenaerts, J. T. M., ... van den Broeke, M. R. (2018). Modelling the climate and surface mass balance of polar ice sheets using racmo2 – part 1: Greenland (1958–2016). *The Cryosphere*, *12*(3), 811–831. Retrieved from `https://tc.copernicus.org/articles/12/811/2018/` doi: 10.5194/tc-12-811-2018

Podolskiy, E., Chambon, G., Naaim, M., & Gaume, J. (2013). A review of finite-element modelling in snow mechanics. *Journal of Glaciology*, *59*(218), 1189–1201. doi: 10.3189/2013JoG13J121

Rew, R., Davis, G., Emmerson, S., Cormack, C., Caron, J., Pincus, R., ... Fisher, W. (1989). *Unidata NetCDF.* UCAR/NCAR - Unidata. Retrieved 2020-09-17, from http://www.unidata.ucar.edu/software/netcdf/ (Language: en Medium: application/java-archive,application/gzip,application/tar) doi: 10.5065/D6H70CW6

Schneider, A. M. (2020, July). *E3SM simulation results and associated python analysis scripts.* Zenodo. Retrieved from https://doi.org/10.5281/zenodo.5950802 (This work is supported by the U.S. Department of Energy's Scientific Discovery Through Advanced Computing (LANL-520117) and Earth System Model Development (DE-SC0019278) programs. Source code was obtained from the Energy Exascale Earth System Model project, sponsored by the U.S. Department of Energy, Office of Science, Office of Biological and Environmental Research. For more information, please contact Adam Schneider (amschnei@uci.edu).) doi: 10.5281/zenodo.5950802

Sellevold, R., & Vizcaíno, M. (2020). Global Warming Threshold and Mechanisms for Accelerated Greenland Ice Sheet Surface Mass Loss. *Journal of Advances in Modeling Earth Systems*, *12*(9), e2019MS002029. Retrieved from https://agupubs.onlinelibrary.wiley.com/doi/abs/10.1029/2019MS002029 (_eprint: https://agupubs.onlinelibrary.wiley.com/doi/pdf/10.1029/2019MS002029) doi: https://doi.org/10.1029/2019MS002029

Steger, C. R., Reijmer, C. H., van den Broeke, M. R., Wever, N., Forster, R. R., Koenig, L. S., ... Noël, B. P. Y. (2017). Firn meltwater retention on the greenland ice sheet: A model comparison. *Frontiers in Earth Science*, *5*, 3. Retrieved from https://www.frontiersin.org/article/10.3389/feart.2017.00003 doi: 10.3389/feart.2017.00003

Stevens, C. M., Verjans, V., Lundin, J. M. D., Kahle, E. C., Horlings, A. N., Horlings, B. I., & Waddington, E. D. (2020). The community firn model (cfm) v1.0. *Geoscientific Model Development*, *13*(9), 4355–4377. Retrieved from https://gmd.copernicus.org/articles/13/4355/2020/ doi: 10.5194/gmd-13-4355-2020

Tuzet, F., Dumont, M., Lafaysse, M., Picard, G., Arnaud, L., Voisin, D., ... Morin, S. (2017). A multilayer physically based snowpack model simulating direct and indirect radiative impacts of light-absorbing impurities in snow. *The Cryosphere*, *11*(6), 2633–2653. Retrieved from https://tc.copernicus.org/articles/11/2633/2017/ doi: 10.5194/tc-11-2633-2017

van Angelen, J. H., van den Broeke, M. R., Wouters, B., & Lenaerts, J. T. M. (2014, September). Contemporary (1960–2012) Evolution of the Climate and Surface Mass Balance of the Greenland Ice Sheet. *Surveys in Geophysics*, *35*(5), 1155–1174. Retrieved from https://doi.org/10.1007/s10712-013-9261-z doi: 10.1007/s10712-013-9261-z

Vandecrux, B., MacFerrin, M., Machguth, H., Colgan, W. T., van As, D., Heilig, A., ... Box, J. E. (2019). Firn data compilation reveals widespread decrease of firn air content in western greenland. *The Cryosphere*, *13*(3), 845–859. Retrieved from https://tc.copernicus.org/articles/13/845/2019/ doi: 10.5194/tc-13-845-2019

van den Broeke, M. (2008). Depth and Density of the Antarctic Firn Layer. *Arctic, Antarctic, and Alpine Research*, *40*(2), 432–438. Retrieved from https://www.tandfonline.com/doi/abs/10.1657/1523-0430%2807-021%29%5BBROEKE%5D2.0.CO%3B2 (Publisher: Taylor & Francis _eprint: https://www.tandfonline.com/doi/pdf/10.1657/1523-0430%2807-021%29%5BBROEKE%5D2.0.CO%3B2) doi: 10.1657/1523-0430(07-021)[BROEKE]2.0.CO;2

van den Broeke, M. R., Enderlin, E. M., Howat, I. M., Kuipers Munneke, P., Noël, B. P. Y., van de Berg, W. J., … Wouters, B. (2016). On the recent contribution of the greenland ice sheet to sea level change. *The Cryosphere*, *10*(5), 1933–1946. Retrieved from https://tc.copernicus.org/articles/10/1933/2016/ doi: 10.5194/tc-10-1933-2016

van Kampenhout, L., Lenaerts, J. T. M., Lipscomb, W. H., Lhermitte, S., Noël, B., Vizcaíno, M., … van den Broeke, M. R. (2020). Present-Day Greenland Ice Sheet Climate and Surface Mass Balance in CESM2. *Journal of Geophysical Research: Earth Surface*, *125*(2), e2019JF005318. Retrieved from https://agupubs.onlinelibrary.wiley.com/doi/abs/10.1029/2019JF005318 (_eprint: https://agupubs.onlinelibrary.wiley.com/doi/pdf/10.1029/2019JF005318) doi: https://doi.org/10.1029/2019JF005318

van Kampenhout, L., Lenaerts, J. T. M., Lipscomb, W. H., Sacks, W. J., Lawrence, D. M., Slater, A. G., & van den Broeke, M. R. (2017). Improving the representation of polar snow and firn in the community earth system model. *Journal of Advances in Modeling Earth Systems*, *9*(7), 2583-2600. Retrieved from https://agupubs.onlinelibrary.wiley.com/doi/abs/10.1002/2017MS000988 doi: https://doi.org/10.1002/2017MS000988

Verjans, V., Leeson, A. A., Nemeth, C., Stevens, C. M., Kuipers Munneke, P., Noël, B., & van Wessem, J. M. (2020). Bayesian calibration of firn densification models. *The Cryosphere*, *14*(9), 3017–3032. Retrieved from https://tc.copernicus.org/articles/14/3017/2020/ doi: 10.5194/tc-14-3017-2020

Verjans, V., Leeson, A. A., Stevens, C. M., MacFerrin, M., Noël, B., & van den Broeke, M. R. (2019). Development of physically based liquid water schemes for greenland firn-densification models. *The Cryosphere*, *13*(7), 1819–1842. Retrieved from https://tc.copernicus.org/articles/13/1819/2019/ doi: 10.5194/tc-13-1819-2019

Vionnet, V., Brun, E., Morin, S., Boone, A., Faroux, S., Le Moigne, P., … Willemet, J.-M. (2012). The detailed snowpack scheme crocus and its implementation in surfex v7.2. *Geoscientific Model Development*, *5*(3), 773–791. Retrieved from https://gmd.copernicus.org/articles/5/773/2012/ doi: 10.5194/gmd-5-773-2012

Viovy, N. (2018). *Cruncep version 7 - atmospheric forcing data for the community land model.* Boulder CO: Research Data Archive at the National Center for Atmospheric Research, Computational and Information Systems Laboratory. Retrieved from https://doi.org/10.5065/PZ8F-F017

Vizcaino, M. (2014). Ice sheets as interactive components of earth system models: progress and challenges. *WIREs Climate Change*, *5*(4), 557-568. Retrieved from https://onlinelibrary.wiley.com/doi/abs/10.1002/wcc.285 doi: https://doi.org/10.1002/wcc.285

WCRP Global Sea Level Budget Group. (2018). Global sea-level budget 1993–present. *Earth System Science Data*, *10*(3), 1551–1590. Retrieved from https://essd.copernicus.org/articles/10/1551/2018/ doi: 10.5194/essd-10-1551-2018